Title

Settling-driven large-scale instabilities in double-diffusive convection

Authors

Ouillon, Raphael
Edel, Philip
Garaud, Pascale
et al.

Publication Date

2020-10-25

DOI

10.1017/jfm.2020.527

Peer reviewed

J. Fluid Mech. (2020), *vol*. 901, A12. © The Author(s), 2020.
Published by Cambridge University Press
doi:10.1017/jfm.2020.527

Settling-driven large-scale instabilities in double-diffusive convection

Raphael Ouillon[1],†, Philip Edel[1,2], Pascale Garaud[3] and Eckart Meiburg[1]

[1]Mechanical Engineering, University of California, Santa Barbara, CA 93106, USA

[2]ENSTA ParisTech, Université Paris-Saclay, Palaiseau, 91120, France

[3]Applied Mathematics, Baskin School of Engineering, University of California, Santa Cruz, CA 95064, USA

(Received 28 February 2020; revised 15 June 2020; accepted 23 June 2020)

When the density of a gravitationally stable fluid depends on a fast diffusing scalar and a slowly diffusing scalar of opposite contribution to the stability, 'double diffusive' instabilities may develop and drive convection. When the slow diffuser settles under gravity, as is for instance the case for small sediment particles in water, settling-driven double-diffusive instabilities can additionally occur. Such instabilities are relevant in a variety of naturally occurring settings, such as particle-laden river discharges, or underground inflows in lakes. Inspired by the dynamics of the more traditional thermohaline double-diffusive instabilities, we ask whether large-scale 'mean-field' instabilities can develop as a result of sedimentary double-diffusive convection. We first apply the mean-field instability theory of Traxler *et al.* (*J. Fluid Mech.*, vol. 677, 2011, pp. 530–553) to high-Prandtl-number fluids, and find that these are unstable to Radko's layering instability, yet collectively stable. We then extend the theory of Traxler *et al.* (2011) to include settling and study its impact on the development of the collective instability. We find that two distinct regimes exist. At low settling velocities, the double-diffusive turbulence in the fingering regime is relatively unaffected by settling and remains stable to the classical collective instability. It is, however, unstable to a new instability in which large-scale gravity waves are excited by the phase shift between the salinity and particle concentration fields. At higher settling velocities, the double-diffusive turbulence is substantially affected by settling, and becomes unstable to the classic collective instability. Our findings, validated by direct numerical simulations, reveal new opportunities to observe settling-driven layering in laboratory and field experiments.

Key words: double diffusive convection, stratified flows, particle/fluid flow

1. Introduction

Double-diffusive convection occurs when the density stratification of a gravitationally stable fluid is caused by the combination of a fast diffusing scalar and a slowly diffusing scalar of opposite contributions to the stability (Stern 1960; Turner 1974; Schmitt 1994; Radko 2013). In the case where the fast and slow diffuser stabilize and destabilize the fluid, respectively, the resulting instability is called 'double-diffusive fingering'.

† Email address for correspondence: raphael.ouillon@gmail.com

In the opposite case, the instability is called 'double-diffusive convection in the diffusive regime'. The necessary conditions for the fingering instability are commonly encountered in the upper layer of the tropical and subtropical ocean, where the temperature and salinity both decrease with depth (You 2002), as well as in the stably stratified regions of stellar interiors (see the review by Garaud 2018). Fingering convection has been the object of much attention in the last 60 years, in laboratory experiments (Turner 1967; Linden 1973; Kunze 2003), theoretical models (Baines & Gill 1969; Schmitt 1979) and direct numerical simulations (Whitfield, Holloway & Holyer 1989; Shen & Schmitt 1995; Merryfield 2000; Stern, Radko & Simeonov 2001; Traxler *et al.* 2011; Radko & Smith 2012). Of particular interest to the present study is the development of secondary, large-scale instabilities from a state of saturated fingering, such as thermohaline staircases (Tait & Howe 1968; Schmitt *et al.* 1987; Krishnamurti 2003; Radko 2003; Stellmach *et al.* 2011) or gravity waves (Stern 1969; Holyer 1981; Traxler *et al.* 2011; Garaud *et al.* 2015). The unified mean-field theory of Traxler *et al.* (2011), following the pioneering efforts of Radko (2003), introduced a general formalism containing all previous theories on large-scale double-diffusive instabilities. However, the theory was originally developed with oceanographic applications in mind, i.e. for the heat-salt system, and therefore does not include settling of one of the scalar fields. The particular case where suspended particles, or sediment, play the role of the slow diffuser is referred to as sedimentary fingering convection (Houk & Green 1973). While qualitatively similar to traditional double-diffusive convection (Green 1987), sedimentary fingering exhibits unique dynamics (Sánchez & Roget 2007; Burns & Meiburg 2012; Yu, Hsu & Balachandar 2013, 2014; Burns & Meiburg 2015; Davarpanah Jazi & Wells 2016; Alsinan, Meiburg & Garaud 2017; Reali *et al.* 2017). The work of Reali *et al.* (2017) was the first and (to the best of the authors' knowledge) the only study to investigate the effect of settling on mean-field instabilities. These authors restricted their analysis to the study of layering instabilities. They found that settling has two complementary effects on layer formation. First, they showed that the settling-induced phase shift between the particle field and the scalar field drives a new mean-field layering instability that is unique to double-diffusive settling. Second, they showed that in some cases, settling can modify the fingering turbulence enough to make it unstable to layering in the traditional sense of Radko (2003). Possible evidence for settling-driven layering was presented in the work of Carazzo & Jellinek (2013), who investigated layer formation in volcanic ash clouds by conducting idealized laboratory experiments in particle-laden salt-stratified water. Their results motivated the theory of Reali *et al.* (2017) at the time, and while the exact mechanism by which layers form in these experiments remains unclear, the possibility of further experiments using a similar set-up prompts us to perform a more comprehensive study of mean-field instabilities in particle-driven double-diffusive convection.

Here, we extend the works of Traxler *et al.* (2011) and Reali *et al.* (2017) to create a unified mean-field theory for large-scale instabilities in sedimentary double-diffusive convection. This unified theory recovers previous mean-field theory results of Stern *et al.* (2001); Radko (2003); Traxler *et al.* (2011) and Reali *et al.* (2017) in various limits. (Traxler *et al.* (2011) further considered lateral gradients, thus allowing their theory to also recover the Walsh & Ruddick (1995) theory of intrusions.) As we shall demonstrate, our work reveals the existence of a new settling-driven collective instability that differs from Stern's particle-free collective instability. Section 2 describes the modelling approach. Section 3 presents the generalized stability analysis of small-scale and mean-field modes. In § 4, we discuss the stability of non-sedimentary systems in the high-Prandtl-number regime and conduct direct numerical simulations (DNS) of a representative problem. In § 5, we analyse the stability of sedimentary systems in the high-Prandtl-number regime

and provide a physical interpretation of the new settling-driven collective instability. We validate our results, at least qualitatively, against DNS. Section 6 concludes with a discussion of the main findings, and how they relate to realistic flows in natural settings.

2. Modelling approach

2.1. *Governing equations*

We model the system using the two-dimensional Navier–Stokes equations in the Boussinesq approximation. Following the same framework as Alsinan *et al.* (2017) and Reali *et al.* (2017), we begin by assuming that the particle concentration field can be modelled as a continuum. We then use the equilibrium Eulerian formalism in which the velocity of the particle field u_p^* is related to the dimensional fluid velocity field $\boldsymbol{u}^*$ (where the asterisk superscript denotes dimensional variables), via

$$\boldsymbol{u}_p^* = \boldsymbol{u}^* - V_{st}\boldsymbol{e}_y, \tag{2.1}$$

where V_{st} is the constant dimensional Stokes settling velocity and $\boldsymbol{e}_y$ is the upward vertical unit vector. For sufficiently spherical particles of density $\rho_p \gg \rho_f$ and radius R,

$$V_{st} = \frac{2}{9}\frac{(\rho_p - \rho_f)}{\rho_f}\frac{gR^2}{\nu}. \tag{2.2}$$

where g is the gravitational acceleration and ν is the kinematic viscosity. The equilibrium Eulerian formalism applies to particulate flows with Stokes number $St = \tau_p/\tau_e \ll 1$, where $\tau_p = V_{st}/g$ is the particle stopping time and $\tau_e = U_{rms}/l$ is the eddy turnover time, with U_{rms} the root-mean-square (r.m.s.) eddy velocity and l the characteristic eddy size (Ferry & Balachandar 2001; Rani & Balachandar 2003). Thus, the applicability of the formalism can only be verified a posteriori, and is discussed for relevant parameters in § 6. We further assume that the particle concentration field, denoted by C^*, can be written as the sum of a time-dependent background $C_0^*(y^*, t^*) = C_m + C_{0y}(y^* + V_{st}^*)$, where C_m is a mean reference density and C_{0y} is the constant background vertical gradient, plus perturbations $\tilde{C}^*$, as

$$C^*(x^*, y^*, t^*) = C_0^*(y^*, t^*) + \tilde{C}^*(x^*, y^*, t^*). \tag{2.3}$$

These particles are embedded in a fluid that is salt stratified, with a constant background vertical gradient of salinity S_{0y}, and with perturbations $\tilde{S}^*$ from that background, so the total salinity field is

$$S^*(x, y, t) = S_0^*(y^*) + \tilde{S}^*(x^*, y^*, t^*), \tag{2.4}$$

where $S_0^*(y^*) = S_m + y^* S_{0y}$ and S_m is a reference salinity. Finally, we use the Boussinesq approximation to relate the total density ρ^* to the salinity and particle concentration as

$$\frac{\rho^* - \rho_0^*}{\rho_f} = \alpha(S^* - S_0^*) + \beta(C^* - C_0^*), \tag{2.5}$$

where ρ_f is the mean fluid density, $\rho_0^*(y^*, t^*)$ is the total density of a fluid of salinity $S_0^*(y^*)$ and particle concentration $C_0^*(y^*, t^*)$, and α and β are constant coefficients related

to derivatives of the equation of state. The set of governing equations is given by

$$\boldsymbol{\nabla}^* \cdot \boldsymbol{u}^* = 0, \tag{2.6}$$

$$\frac{\partial \boldsymbol{u}^*}{\partial t^*} + (\boldsymbol{u}^* \cdot \boldsymbol{\nabla}^*)\boldsymbol{u}^* = -\frac{1}{\rho_f}\boldsymbol{\nabla}^*\tilde{p}^* + \nu \Delta^* \boldsymbol{u}^* - (\alpha \tilde{S}^* + \beta \tilde{C}^*) g \boldsymbol{e}_y, \tag{2.7}$$

$$\frac{\partial \tilde{C}^*}{\partial t^*} + \boldsymbol{u}^* \cdot \boldsymbol{\nabla}^* \tilde{C}^* + \tilde{v}^* C_{0y} - V_{st}\frac{\partial \tilde{C}^*}{\partial y^*} = \kappa_c \Delta^* \tilde{C}^*, \tag{2.8}$$

$$\frac{\partial \tilde{S}^*}{\partial t^*} + \boldsymbol{u}^* \cdot \boldsymbol{\nabla}^* \tilde{S}^* + \tilde{v}^* S_{0y} = \kappa_s \Delta^* \tilde{S}^*. \tag{2.9}$$

where $\boldsymbol{u}^* = (u^*, v^*)$, $\tilde{p}^*$ is the dimensional pressure perturbation from the background state, $\boldsymbol{g} = -g\boldsymbol{e}_y$ is the acceleration due to gravity ($g \approx 9.81\ \mathrm{m\,s^{-2}}$), ν is the kinematic viscosity ($\nu \approx 10^{-6}\ \mathrm{m^2\,s^{-1}}$) and κ_s and κ_c are the salt and particle diffusivities, respectively. While the molecular diffusivity of salt ions is typically $\kappa_s \approx 10^{-9}\ \mathrm{m^2\,s^{-1}}$ (Poisson & Papaud 1983), the hydrodynamic diffusivity of particles is more difficult to characterize as it varies markedly with the hydrodynamic conditions of the suspension, the shear experienced by the particles, the particle volume fraction, as well as the size of the particles (Davis 1996). However, for very small and non-inertial particles that thus fall within the limits of applicability of the equilibrium Eulerian description of particle transport, the particle diffusivity is very small and $\kappa_c/\kappa_s \ll 1$. We note that this assumption breaks down when hard boundaries are present in the fluid domain and particles are allowed to accumulate, and that the suspension is therefore not locally dilute. Here, however, all perturbations to the background state are assumed to be doubly periodic, to eliminate any contamination by boundary conditions.

2.2. *Non-dimensional equations*

The governing equations (2.6)–(2.9) are made non-dimensional using the anticipated finger scale $d = (\nu\kappa_s/\alpha g|S_{0y}|)^{1/4} = (\nu\kappa_s/N^2)^{1/4}$, following standard practice (Radko 2013), where N is the local buoyancy frequency associated with the salt stratification. A velocity scale $U = \kappa_s/d$ and time scale $T = d^2/\kappa_s$ are then introduced based on the diffusivity of the fast diffuser. The salinity and particle concentration fields are non-dimensionalized using $d|S_{0y}|$ and $(\alpha/\beta)d|S_{0y}|$ respectively. By choosing $P = \rho_f \nu\kappa_s/d^2$ as the pressure scale, the non-dimensional equations become

$$\boldsymbol{\nabla} \cdot \boldsymbol{u} = 0, \tag{2.10}$$

$$\frac{1}{Pr}\left(\frac{\partial \boldsymbol{u}}{\partial t} + (\boldsymbol{u} \cdot \boldsymbol{\nabla})\boldsymbol{u}\right) = -\boldsymbol{\nabla}\tilde{p} + \Delta \boldsymbol{u} - \left(\tilde{S} + \tilde{C}\right)\boldsymbol{e}_y, \tag{2.11}$$

$$\frac{\partial \tilde{C}}{\partial t} + \boldsymbol{u} \cdot \boldsymbol{\nabla}\tilde{C} + \frac{v}{R_0} - V\frac{\partial \tilde{C}}{\partial y} = \tau \Delta \tilde{C}, \tag{2.12}$$

$$\frac{\partial \tilde{S}}{\partial t} + \boldsymbol{u} \cdot \boldsymbol{\nabla}\tilde{S} - v = \Delta \tilde{S}, \tag{2.13}$$

where all quantities have now been non-dimensionalized, and where $\tau = \kappa_c/\kappa_s$ is the diffusivity ratio, $Pr = \nu/\kappa_s$ ($\approx 10^3$) is the Prandtl number (although it is understood here as a Schmidt number, we choose to call it a Prandtl number in order to stay consistent with the existing literature on double diffusion, which is mainly focused on heat-salt

systems) and $V = V_{st}d/\kappa_s$ is the non-dimensional settling velocity. The density ratio is $R_0 = \alpha|S_{0y}|/\beta|C_{0y}|$.

The system (2.10)–(2.13) is identical to that of Alsinan *et al.* (2017), with the only exception that the authors considered a temperature–particle system. This impacts the signs of the dimensional background gradients S_{0y} and C_{0y}, leading to sign differences in the non-dimensional perturbation equations. For consistency with the literature (Traxler *et al.* 2011; Alsinan *et al.* 2017; Reali *et al.* 2017), we define a new variable $\tilde{\Theta}$ analogous to the temperature in classic double-diffusive convection as $\tilde{\Theta} = -\tilde{S}$. This allows us to re-write (2.10)–(2.13) as

$$\boldsymbol{\nabla}\cdot\boldsymbol{u} = 0, \tag{2.14}$$

$$\frac{1}{Pr}\left(\frac{\partial \boldsymbol{u}}{\partial t} + (\boldsymbol{u}\cdot\boldsymbol{\nabla})\boldsymbol{u}\right) = -\boldsymbol{\nabla}\tilde{p} + \Delta\boldsymbol{u} + (\tilde{\Theta} - \tilde{C})\boldsymbol{e}_y, \tag{2.15}$$

$$\frac{\partial \tilde{C}}{\partial t} + \boldsymbol{u}\cdot\boldsymbol{\nabla}\tilde{C} + \frac{v}{R_0} - V\frac{\partial \tilde{C}}{\partial y} = \tau\Delta\tilde{C}, \tag{2.16}$$

$$\frac{\partial \tilde{\Theta}}{\partial t} + \boldsymbol{u}\cdot\boldsymbol{\nabla}\tilde{\Theta} + v = \Delta\tilde{\Theta}. \tag{2.17}$$

This model is now identical to the system of equations used by Alsinan *et al.* (2017) and Reali *et al.* (2017), and further reduces to the standard double-diffusive equations when $V = 0$ (Radko 2013). Since the salt diffusivity is much smaller than the temperature diffusivity, the typical values of the finger width, unit time scale and unit velocity differ from those discussed by Alsinan *et al.* (2017). In particular, using a fiducial value of $N \sim 10^{-2}\ \mathrm{s}^{-1}$, we find that $d \sim 1.8$ mm, $d^2/\kappa_s \sim 53$ min and $\kappa_s/d \sim 5.6\times10^{-7}\ \mathrm{m\,s}^{-1}$.

2.3. *Numerical method*

These equations were solved using two independently developed doubly periodic codes. In the results presented in §§ 3 and 4 we used a two-dimensional hybrid pseudo-spectral compact finite difference spatial scheme combined with a low-storage Runge–Kutta/Crank–Nicolson time-stepping method. The algorithm ensures incompressibility by recasting the problem in terms of a streamfunction and the vorticity, which are related by a Poisson equation. This code was designed to run efficiently on massively parallel supercomputers using the *MPI* and *FFTW* libraries. Small-scale simulations were run on 12 cores on a local server while large-scale simulations were run on up to 2048 cores on the TACC Stampede2 supercomputer. In the results presented in § 5, we used the PADDI code (Stellmach *et al.* 2011; Traxler *et al.* 2011; Reali *et al.* 2017), which is a pseudo-spectral algorithm based on the classical Patterson–Orszag method (Canuto *et al.* 2007). A third-order semi-implicit Adams–Bashforth/backward-differencing algorithm is used for time stepping (Peyret 2002). Advection terms are treated explicitly and diffusion terms are treated implicitly. PADDI employs an adaptive time-step method to guarantee stability. The code was also designed to run efficiently on massively parallel supercomputers and employs a transpose-based parallel transform algorithm (Stellmach & Hansen 2008).

The codes were cross-validated by comparing their results on small-domain experiments reported in table 1. All domain-averaged and time-averaged quantities were found to be statistically consistent between the two codes.

3. Generalized stability analysis

3.1. *Small-scale instability*

In the absence of settling, a linear stability analysis of the non-dimensional equations (2.14)–(2.17) yields the well-known instability condition for double-diffusive fingering, i.e. that $R_0 < 1/\tau$ (Radko 2013). Alsinan *et al.* (2017) studied the linear stability of the same equations in the presence of settling by linearizing the governing equations and using normal modes of the form

$$\left(u, v, \tilde{p}, \tilde{\Theta}, \tilde{C}\right) \sim \mathrm{Re}\left(\left(\hat{u}, \hat{v}, \hat{p}, \hat{\Theta}, \hat{C}\right) \exp(\lambda t + \mathrm{i}lx + \mathrm{i}ky)\right), \tag{3.1}$$

where $\lambda \in \mathbb{C}$ is the complex growth rate, l the horizontal wavenumber and k the vertical wavenumber (so as to be consistent with the literature, see Alsinan *et al.* 2017). The resulting cubic equation for the growth rate of small-scale instabilities in the presence of settling is found to be

$$\lambda^3 + c_2\lambda^2 + c_1\lambda + c_0 = 0, \tag{3.2}$$

where

$$c_2 = (1 + \tau + Pr)|\boldsymbol{k}|^2 - \mathrm{i}kV, \tag{3.3a}$$

$$c_1 = (\tau + Pr + \tau Pr)|\boldsymbol{k}|^4 + \frac{Pr\, l^2}{|\boldsymbol{k}|^2}(1 - R_0^{-1}) - \mathrm{i}kV|\boldsymbol{k}|^2(1 + Pr), \tag{3.3b}$$

$$c_0 = \tau Pr|\boldsymbol{k}|^6 - Pr\, l^2\left(R_0^{-1} - \tau\right) - \frac{\mathrm{i}kVPr}{|\boldsymbol{k}|^2}\left(l^2 + |\boldsymbol{k}|^6\right), \tag{3.3c}$$

and $|\boldsymbol{k}|^2 = k^2 + l^2$. Alsinan *et al.* (2017) showed that settling excites a new mode of instability that exists at all density ratios. The mode is an inclined gravity wave, and is excited even when the two scalars diffuse at identical rates. If the scalar components have unequal diffusivities, the settling-driven instability competes with the classical fingering instability.

3.2. *Mean-field theory*

Large-scale structures such as intrusions, internal gravity waves or layers, can spontaneously emerge from homogeneous fingering convection (Merryfield 2000; Stern *et al.* 2001; Radko 2003; Stellmach *et al.* 2011; Traxler *et al.* 2011). Mean-field models have been employed to investigate the formation mechanism of these structures, under the foundational assumption that they operate on scales much larger than that of individual fingers. By considering a local average over several finger widths, we can construct the evolution equations of the large-scale fields and analyse their linear stability following the work of Traxler *et al.* (2011). The averaging operator, marked as $\bar{\cdot}$, is assumed to commute with temporal and spatial differentiation operators. Each field $\boldsymbol{u}$, $\tilde{p}$, $\tilde{\Theta}$ and $\tilde{C}$ can be separated into average and fluctuating quantities, i.e.

$$\boldsymbol{u} = \bar{\boldsymbol{u}} + \boldsymbol{u}', \quad \tilde{p} = \bar{p} + p', \quad \tilde{\Theta} = \overline{\Theta} + \Theta' \quad \text{and} \quad \tilde{C} = \overline{C} + C', \tag{3.4a–d}$$

such that $\bar{\boldsymbol{u}'} = \overline{p'} = \overline{\Theta'} = \overline{C'} = 0$. We introduce the turbulent flux of particles defined as $\boldsymbol{F}_c = \overline{\boldsymbol{u}'C'}$, the turbulent flux of salinity (or, to be precise, minus the salinity) defined as $\boldsymbol{F}_\theta = \overline{\boldsymbol{u}'\Theta'}$ and the Reynolds stress tensor defined as $\boldsymbol{R}_{ij} = \overline{u_i'u_j'}$. Following Traxler *et al.* (2011), two hypotheses are made: (i) the Reynolds stress term is small and can be neglected

and (ii) the vertical turbulent fluxes of particles and salt $F_c = \overline{v'C'}$ and $F_\theta = \overline{v'\Theta'}$ are much more significant than the horizontal fluxes $\overline{u'C'}$ and $\overline{u'\Theta'}$, such that $\boldsymbol{F}_c \approx F_c \boldsymbol{e}_y$ and $\boldsymbol{F}_\theta \approx F_\theta \boldsymbol{e}_y$. Note that both assumptions are only true in the absence of lateral gradients that would otherwise drive intrusions (Walsh & Ruddick 1995; Rudnick 1999). Under these assumptions, the averaged governing equations are given by

$$\boldsymbol{\nabla} \cdot \bar{\boldsymbol{u}} = 0, \tag{3.5}$$

$$\frac{1}{Pr}\left(\frac{\partial \bar{\boldsymbol{u}}}{\partial t} + (\bar{\boldsymbol{u}} \cdot \boldsymbol{\nabla})\bar{\boldsymbol{u}}\right) = -\boldsymbol{\nabla}\bar{p} + \Delta \bar{\boldsymbol{u}} + (\overline{\Theta} - \overline{C})\boldsymbol{e}_y, \tag{3.6}$$

$$\frac{\partial \overline{C}}{\partial t} + \bar{\boldsymbol{u}} \cdot \boldsymbol{\nabla}\overline{C} + \frac{\overline{v}}{R_0} - V\frac{\partial \overline{C}}{\partial y} + \frac{\partial F_c}{\partial y} = \tau \Delta \overline{C}, \tag{3.7}$$

$$\frac{\partial \overline{\Theta}}{\partial t} + \bar{\boldsymbol{u}} \cdot \boldsymbol{\nabla}\overline{\Theta} + \overline{v} + \frac{\partial F_\theta}{\partial y} = \Delta \overline{\Theta}. \tag{3.8}$$

In order to express the flux terms $\partial F_c/\partial y$ and $\partial F_\theta/\partial y$ as functions of the mean-field parameters, we introduce, as in Radko (2003), the Nusselt number Nu and turbulent flux ratio γ, as

$$Nu = \frac{F_\theta - \left(1 + \dfrac{\partial \overline{\Theta}}{\partial y}\right)}{-\left(1 + \dfrac{\partial \overline{\Theta}}{\partial y}\right)} \quad \text{and} \quad \gamma = \frac{F_\theta}{F_c}. \tag{3.9a,b}$$

The Nusselt number is to be understood as the ratio of the total salt (or pseudo-temperature) flux $F_\theta^{tot} = F_\theta - (1 + \partial\overline{\Theta}/\partial y)$ (taking into account both turbulent fluctuation and molecular fluxes) to the molecular salt flux. The particle and salt turbulent fluxes can thus be expressed as

$$F_\theta = (1 - Nu)\left(1 + \frac{\partial \overline{\Theta}}{\partial y}\right), \tag{3.10}$$

$$F_c = \frac{1}{\gamma}(1 - Nu)\left(1 + \frac{\partial \overline{\Theta}}{\partial y}\right). \tag{3.11}$$

The key hypothesis of the mean-field theory (Radko 2003; Traxler *et al.* 2011) resides in assuming that for given values of Pr, τ and V, the quantities Nu and γ depend only on the local density ratio R_ρ, defined as

$$R_\rho = R_0\left(\frac{1 + \dfrac{\partial \overline{\Theta}}{\partial y}}{1 + R_0\dfrac{\partial \overline{C}}{\partial y}}\right). \tag{3.12}$$

Note that the validity of this assumption crucially depends on the fingers being short compared with the typical length scale of variation of $\overline{\Theta}$ and $\overline{C}$. By assuming that

$R_0(\partial\overline{C}/\partial y) \ll 1$ we can linearize this expression to obtain

$$R_\rho = R_0 + R'_\rho \tag{3.13}$$

where

$$R'_\rho = R_0\left(\frac{\partial\overline{\Theta}}{\partial y} - R_0\frac{\partial\overline{C}}{\partial y}\right). \tag{3.14}$$

It then follows that

$$Nu(R_\rho) \approx Nu(R_0) + \left.\frac{\mathrm{d}Nu}{\mathrm{d}R_\rho}\right|_{R_0} R'_\rho, \tag{3.15}$$

$$\frac{1}{\gamma(R_\rho)} \approx \frac{1}{\gamma(R_0)} + \left.\frac{\mathrm{d}(1/\gamma)}{\mathrm{d}R_\rho}\right|_{R_0} R'_\rho. \tag{3.16}$$

By inserting these expressions into (3.10) we finally obtain linearized expressions for the turbulent fluxes

$$F_\theta = -A_2\left(\frac{\partial\overline{\Theta}}{\partial y} - R_0\frac{\partial\overline{C}}{\partial y}\right) - (Nu_0 - 1)\left(1 + \frac{\partial\overline{\Theta}}{\partial y}\right), \tag{3.17}$$

$$F_c = -A_1\left(\frac{\partial\overline{\Theta}}{\partial y} - R_0\frac{\partial\overline{C}}{\partial y}\right)(Nu_0 - 1) + \frac{1}{\gamma_0}F_\theta, \tag{3.18}$$

where we have introduced the four constants

$$Nu_0 = Nu(R_0), \quad \gamma_0 = \gamma(R_0), \quad A_1 = R_0\left.\frac{\mathrm{d}(1/\gamma)}{\mathrm{d}R_\rho}\right|_{R_0} \quad \text{and} \quad A_2 = R_0\left.\frac{\mathrm{d}Nu}{\mathrm{d}R_\rho}\right|_{R_0}. \tag{3.19a–d}$$

The system of (3.5)–(3.8) can now be linearized to

$$\frac{\partial\overline{u}}{\partial x} + \frac{\partial\overline{v}}{\partial y} = 0, \tag{3.20}$$

$$\left(\frac{1}{Pr}\frac{\partial}{\partial t} - \Delta\right)\left(\frac{\partial\overline{u}}{\partial y} - \frac{\partial\overline{v}}{\partial x}\right) + \frac{\partial\overline{\Theta}}{\partial x} - \frac{\partial\overline{C}}{\partial x} = 0, \tag{3.21}$$

$$\frac{\partial\overline{C}}{\partial t} + \frac{\overline{v}}{R_0} - V\frac{\partial\overline{C}}{\partial y} + \frac{1}{\gamma_0}\left(\Delta\overline{\Theta} - \overline{v} - \frac{\partial\overline{\Theta}}{\partial t}\right) - A_1\left(\frac{\partial^2\overline{\Theta}}{\partial y^2} - R_0\frac{\partial^2\overline{C}}{\partial y^2}\right)(Nu_0 - 1) - \tau\Delta\overline{C} = 0, \tag{3.22}$$

$$\frac{\partial\overline{\Theta}}{\partial t} + \overline{v} - (Nu_0 - 1)\frac{\partial^2\overline{\Theta}}{\partial y^2} - A_2\left(\frac{\partial^2\overline{\Theta}}{\partial y^2} - R_0\frac{\partial^2\overline{C}}{\partial y^2}\right) - \Delta\overline{\Theta} = 0. \tag{3.23}$$

The linear stability of these equations is then examined by using normal modes in the form

$$\left(\overline{u}, \overline{v}, \overline{\Theta}, \overline{C}\right) \sim \mathrm{Re}\left((\hat{u}, \hat{v}, \hat{\Theta}, \hat{C})\exp(\lambda t + \mathrm{i}lx + \mathrm{i}ky)\right), \tag{3.24}$$

where $\lambda \in \mathbb{C}$ is the complex growth rate and l and k are horizontal and vertical wavenumbers, respectively. After a series of algebraic manipulations, we obtain the

following cubic eigenvalue equation

$$\lambda^3 + a_2\lambda^2 + a_1\lambda + a_0 = 0, \tag{3.25}$$

where

$$a_2 = b_1 + Pr|\boldsymbol{k}|^2, \tag{3.26}$$

$$a_1 = b_2 + Pr|\boldsymbol{k}|^2 b_1 + Pr\frac{l^2}{|\boldsymbol{k}|^2}\left(1 - \frac{1}{R_0}\right), \tag{3.27}$$

$$a_0 = Pr|\boldsymbol{k}|^2 b_2 + Pr\frac{l^2}{|\boldsymbol{k}|^2}\left[|\boldsymbol{k}|^2\left(\tau - \frac{1}{R_0}\right) + \left(\frac{1}{\gamma_0} - \frac{1}{R_0}\right)(A_2(1-R_0) + Nu_0 - 1)\,k^2 + A_1k^2(Nu_0 - 1)(1 - R_0) - \mathrm{i}kV\right], \tag{3.28}$$

and

$$b_1 = (1+\tau)|\boldsymbol{k}|^2 + k^2\left(A_2\left(1 - \frac{R_0}{\gamma_0}\right) + (Nu_0 - 1)(1 - A_1R_0)\right) - \mathrm{i}kV, \tag{3.29}$$

$$b_2 = \left(|\boldsymbol{k}|^2 + k^2(A_2 + Nu_0 - 1)\right)\left(\tau|\boldsymbol{k}|^2 - A_1R_0k^2(Nu_0 - 1) - \mathrm{i}kV\right) + A_2R_0k^2\left(A_1k^2(Nu_0 - 1) - \frac{|\boldsymbol{k}|^2}{\gamma_0}\right). \tag{3.30}$$

In the absence of settling ($V = 0$) we recover the real coefficients of the cubic equation from Traxler *et al.* (2011, equation (2.13*a–c*)) (after setting $m = 0$, i.e. in the two-dimensional form of the cubic equation). Settling causes these coefficients to become complex. When only considering the horizontally invariant $l = 0$ modes, we recover the cubic equation of Reali *et al.* (2017). Note that the roots of the polynomial depend explicitly on the mean-field parameters Nu_0, γ_0, A_1 and A_2, all of which are functions of the fluxes $F_c = \overline{v'C'}$ and $F_\theta = \overline{v'\Theta'}$. Therefore, determination of the growth rate of the mean-field modes of instability for any given system (Pr, τ, R_0, V) first requires knowledge of the turbulent fluxes associated with the small-scale fingering. The latter can be obtained through small-domain nonlinear simulations of the full set of equations as in, e.g. Traxler *et al.* (2011), or Reali *et al.* (2017); see appendix A for more on this topic.

Mean-field theory predicts the existence of several large-scale instabilities. Intrusions require horizontal gradients of the background fields (Walsh & Ruddick 1995) and are thus not considered here. The collective instability, as derived in the work of Stern *et al.* (2001), is obtained in the limit of discarding the diffusion terms for the diffusing scalar fields and neglecting the possible dependence of γ on R_0 (i.e. $A_1 = 0$). In the absence of settling, the collective instability is known to excite internal gravity waves.

The γ-instability, first derived in Radko (2003) in the absence of settling and later generalized in the presence of settling in Reali *et al.* (2017), is obtained when considering horizontally invariant perturbations ($l = 0$) with zero mean flow. The averaged equations (3.5)–(3.8) then become

$$\frac{\partial\overline{C}}{\partial t} = -\frac{\partial F_c^{tot}}{\partial y} + V\frac{\partial\overline{C}}{\partial y}, \tag{3.31}$$

$$\frac{\partial\overline{\Theta}}{\partial t} = -\frac{\partial F_\theta^{tot}}{\partial y}, \tag{3.32}$$

where $F_\theta^{tot} = F_\theta - (-1 + \partial\overline{\Theta}/\partial y)$ and $F_c^{tot} = F_c - \tau(1/R_0 + \partial\overline{C}/\partial y)$ are particle and salt total fluxes, which take into account both fluctuation and molecular components. These total fluxes are introduced for the sake of consistency with the literature. The total flux ratio is

$$\gamma^{tot} = \frac{F_\theta^{tot}}{F_c^{tot}}, \tag{3.33}$$

which is again assumed to depend only on the local density ratio R_ρ.

Radko (2003) showed that a necessary condition for the layering instability is that γ^{tot} should be a decreasing function of R_ρ, hence the name 'γ-instability'. Reali *et al.* (2017) showed that with added settling, there are two ways in which layering is possible. Firstly, for certain settling rates, settling can modify the turbulence in such a way that γ^{tot} becomes a decreasing function of R_ρ even when it was not in the absence of settling, thus leading to the classic γ-instability. Secondly, a new layering instability can occur even when γ^{tot} is an increasing function of R_ρ and thus differs from the γ-instability.

4. High-Prandtl-number non-sedimentary systems

4.1. *Collective stability in γ-unstable systems*

On the way to studying mean-field instabilities of high-Prandtl-number sedimentary systems, we begin by investigating the case without settling for comparison and completeness. As an illustration, we consider a system whose parameters are $R_0 = 1.5$, $Pr = 200$, $\tau = 0.1$ which we will write as $\Sigma_{num} = (R_0 = 1.5, Pr = 200, \tau = 0.1)$ for convenience.

We begin by running small-domain simulations at these parameters. As described in appendix A, the domain size is 37×74 units of length (corresponding to roughly 5×10 fgw, where 1 fgw is 1 wavelength of the fastest-growing mode) and we choose a grid of 256×512 grid points. Given that $R_0 < 1/\tau$ in the system Σ_{num}, it is known to be unstable to the fingering instability as confirmed by the formation of particle-rich fingers at the beginning of the simulations (figure 1*a*). The fingers eventually saturate to form a homogeneous and statistically stationary state of fingering convection (figure 1*b*) during which the fluxes are measured, and used to compute the mean-field parameters Nu_0, γ_0, γ^{tot}, A_1, A_2 and A_1^{tot} (see table 1, first row).

Note that two-dimensional simulations are known to underestimate the fluxes compared to more realistic three-dimensional simulations (Stern *et al.* 2001; Reali *et al.* 2017). As such, they cannot be used to study the problem quantitatively, but provide an acceptable tool for a qualitative exploration of the mean-field stability of the system (Traxler *et al.* 2011).

From table 1 (first row), we find that the condition for γ-instability $A_1^{tot} > 0$ is satisfied at the Σ_{num} parameters. More surprisingly, the system is also found to be stable to the collective instability. This is seen by solving the general cubic equation (3.25) for the mean-field mode growth rate λ, using the measured mean-field parameter values Nu_0, γ_0, A_1 and A_2, and plotting the resulting positive real part of the growth rate in the so-called 'flower plot' (see Traxler *et al.* 2011), in which the horizontal wavenumber is plotted on the y-axis, and the vertical wavenumber is plotted in the x-axis. Figure 2 juxtaposes the positive real part of the basic instability growth rate obtained by solving the cubic equation (3.2), in the left image, with the positive real part of the growth rate of mean-field modes of instability, obtained by solving the cubic equation (3.25), in the right image. Here, we use the fact that in the absence of horizontal gradients, the real part of λ is symmetric about $k = 0$, and only present the half-flower plot of both cubics. We see that the basic modes (*a*)

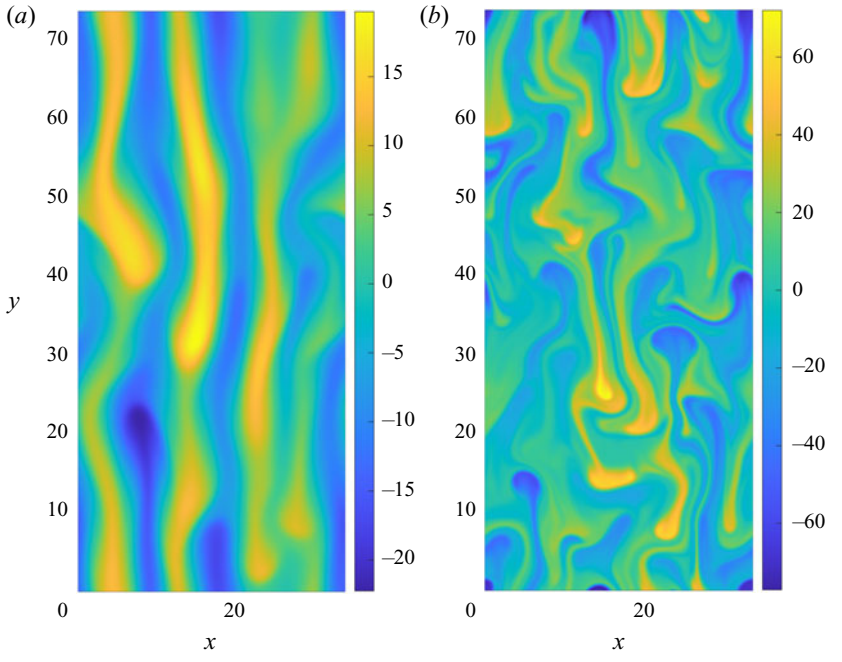

FIGURE 1. Snapshots of the concentration perturbation $\tilde{C}$ in small-scale simulation of the $\Sigma_{num} = (R_0 = 1.5, Pr = 200, \tau = 0.1)$ system at $V = 0$. (*a*) Double-diffusive fingers in the concentration field at early times. (*b*) Concentration field in the statistically stationary state of fingering convection. (*a*) $t = 33$, (*b*) $t = 45$.

V	Nu_0	γ_0	γ^{tot}	A_2	A_1	A_1^{tot}
0	76.4 ± 7.0	0.684 ± 0.02	0.693 ± 0.02	-447.8 ± 134.8	0.58	0.47
0.25	73.5 ± 6.5	0.680 ± 0.02	0.689 ± 0.02	-439.8 ± 138.3	0.55	0.44
0.5	77.4 ± 6.0	0.680 ± 0.01	0.688 ± 0.01	-428.1 ± 111.8	0.53	0.42
0.7	79.0 ± 8.1	0.674 ± 0.02	0.682 ± 0.02	-470.4 ± 156.0	0.53	0.42
0.9	77.3 ± 6.5	0.669 ± 0.02	0.678 ± 0.02	-443.4 ± 191.0	0.35	0.27
1	83.6 ± 8.6	0.666 ± 0.02	0.674 ± 0.02	-478.3 ± 143.9	0.60	0.49
1.5	99.0 ± 12.8	0.655 ± 0.03	0.662 ± 0.02	-599.5 ± 238.2	0.68	0.58
2	107.1 ± 13.6	0.632 ± 0.03	0.628 ± 0.03	-720.7 ± 185.6	0.85	0.76
5	234.7 ± 38.4	0.556 ± 0.05	0.554 ± 0.05	-798.1 ± 97.1	0.362	0.355
10	486.6 ± 117.9	0.475 ± 0.12	0.474 ± 0.12	-1986.6 ± 465.1	0.463	0.459

TABLE 1. Estimates of mean-field parameters for Σ_{num} for different settling velocities V.

are unstable for most values of k and l at high Pr. Interestingly, we see that a substantial proportion of these modes are stabilized in the mean-field theory (*b*). The γ-instability appears at very low values of l, and the collective modes, had they been present, would appear as leaves (Traxler *et al.* 2011). The Σ_{num} system without settling can therefore be characterized as (i) unstable to the fingering instability, (ii) collectively stable and (iii) γ-unstable. This is highly unusual since, to our knowledge, γ-unstable systems have only

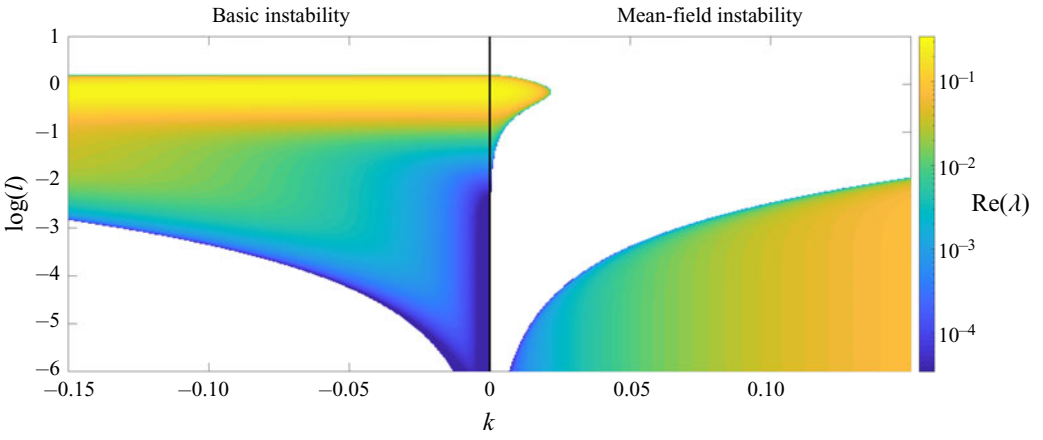

FIGURE 2. Real part of growth rates for the fastest-growing perturbations for Σ_{num} with $V = 0$. The left-hand side is calculated using the basic instability cubic equation (3.2) while the right-hand side corresponds to the growth rates calculated using the generalized mean-field theory, see (3.25). Here, we use the symmetry with respect to $k = 0$ to only represent half of the wavenumber space of each solution. Note that the plot uses a logarithmic colour scale.

ever been found so far in collectively unstable systems (Radko 2003; Traxler *et al.* 2011; Garaud *et al.* 2015).

4.2. *DNS results*

Large-scale simulations of the Σ_{num} system in the absence of settling are carried out to investigate the long-term evolution of the fingering convection, and to study the resulting large-scale instabilities predicted to occur from the mean-field theory. This time, the domain width is $L_x = 20$ fgw, and the domain height is $L_y = 40$ fgw, thus containing the equivalent of 16 small-scale 5×10 fgw domains.

Figure 3 shows snapshots of the concentration perturbation field $\tilde{C}$ throughout the simulation. First, thin elongated particle-rich fingers appear ($t = 30$), rapidly followed by a long-lasting homogeneous state of fingering convection ($t = 50$) which remains until layering begins ($t = 2750$), and becomes established ($t = 3200$). This result is of particular importance as it confirms the hypothesis of Radko (2003) that collective instabilities are not required for the γ-instability to generate layers.

The amplitude of the Fourier coefficient of the particle concentration field $|\hat{C}(l, k)|$, for the first three layering modes (also called $\gamma-$modes), i.e. modes with wavenumber $\boldsymbol{k} = (0, k_1)$, $(0, k_2)$ and $(0, k_3)$, where $k_n = 2n\pi/L_y$ denotes the vertical wavenumber, is shown in figure 4. The exponential growth of $(0, k_1)$, starting at $t = 1100$ is characteristic of γ-instabilities (Radko 2003; Stellmach *et al.* 2011).

Solving the mean-field eigenvalue cubic equation (3.25) for the same three γ-modes, we find growth rates of 0.0023 for $(0, k_1)$, 0.0091 for $(0, k_2)$ and 0.020 for $(0, k_3)$. The measured growth rate of the $(0, k_1)$ mode in the DNS is 0.00145, which agrees relatively well with the predicted value of 0.0023. However, the $(0, k_2)$ and $(0, k_3)$ modes, which are actually predicted to grow more rapidly than the $(0, k_1)$ mode have negligible growth rates (see figure 2). Our hypothesis for the discrepancy between the mean-field theory and the DNS is that, at such high Prandtl numbers, the fingers remain vertically coherent over large length scales, which invalidates the local assumption made in the mean-field

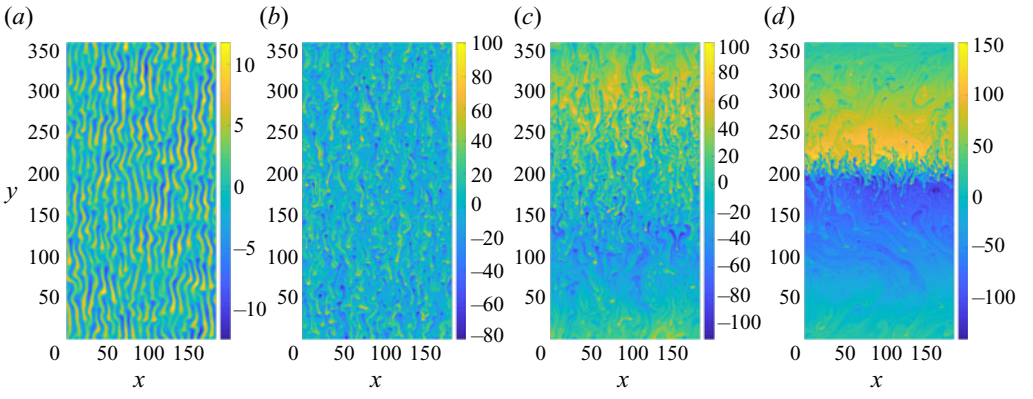

FIGURE 3. Large-scale DNS for $V = 0$, Σ_{num}. Snapshots of the particle concentration perturbation field $\tilde{C}$ at $t = 30$ (beginning of fingering), $t = 50$ (established fingering convection), $t = 2750$ (onset of layering) and at $t = 3200$ (layering is established).

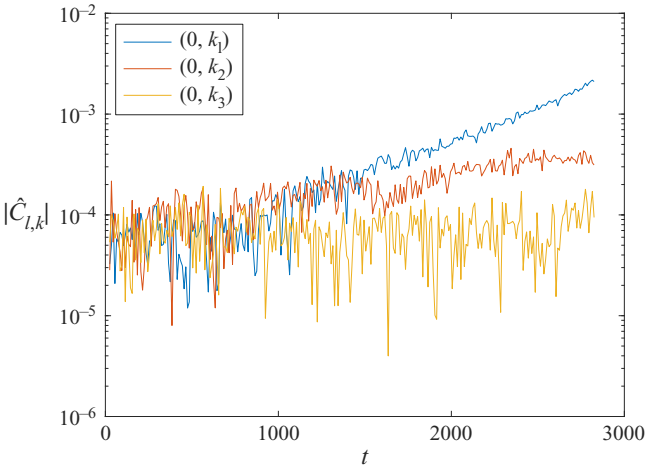

FIGURE 4. Times series of the amplitude of the Fourier mode $\hat{C}(l, k)$ of the particle concentration field for layer modes $(0, k_1)$, $(0, k_2)$ and $(0, k_3)$ in the $V = 0$ Σ_{num} large-scale DNS discussed in § 4.2.

approximation. From figure 3, we can estimate the length of the fingers to be approximately (20–50)d. It was observed by Stellmach *et al.* (2011) that the growth rate of the collective instability is accurately predicted only for modes whose characteristic length is larger than approximately 5 fingers. Here, it appears that the elongated fingers also affect the growth of the γ-modes, where layers thinner than 5 finger heights (or up to approximately 250d) are unable to grow at the predicted rate.

In summary, we find that non-sedimentary high-Prandtl-number systems can be collectively stable yet unstable to γ-modes, and confirmed with DNS that layering can occur in the absence of gravity waves. Such an observation had yet to be made and further confirms the role of the γ-instability introduced by Radko (2003) on layering in double-diffusive systems.

5. High-Prandtl-number sedimentary systems

5.1. *A settling-driven collective instability*

Building on the results of § 4, we now include sedimentary effects by allowing the particles to settle at a non-dimensional velocity V, varied between $V = 0$ and $V = 10$. As before, we first run numerous small-scale simulations to estimate mean-field parameters for different values of V (summarized in table 1), and then solve the cubic equation (3.25) to find the respective growth rates of various mean-field modes of instability. We focus here on the same basic parameters as in § 4, namely $R_0 = 1.5$, $Pr = 200$ and $\tau = 0.1$. Figure 5 juxtaposes the positive real part of the basic instability growth rate obtained by solving the cubic equation (3.2), in the left image, with the positive real part of the growth rate of mean-field modes of instability, obtained by solving the cubic equation (3.25), in the right image. Two values of the settling velocity are shown, from top to bottom, for $V = 2$ and 10. As in figure 2, we use the fact that in the absence of horizontal gradients, the real part of λ is symmetric about $k = 0$, and only present the half-flower plot of both cubics.

At $V = 2$, the mean-field theory now predicts the existence of an additional large-scale oscillatory mode (the leaf of the flower) that was not present at $V = 0$ (see figure 2), suggesting that settling plays a role in driving it. The fastest-growing modes in the leaf at these parameters have vertical wavenumbers $k = O(10^{-2})$ and horizontal wavenumbers $l < O(10^{-2})$. Without further information, however, it is not entirely clear that these modes are genuine mean-field modes, or basic modes that are *not* suppressed in the mean-field theory when $V \neq 0$. At $V = 10$, however, the oscillatory mean-field modes admit a maximum growth rate that is much larger than that of the basic modes at the same wavenumbers. Contours of the growth rate predicted by the mean-field theory have been added to figure 5 for $V = 10$ on both sides of the flower plot to better visualize the offset between the mean-field, settling-driven unstable modes and the basic modes. This suggests that the unstable region indeed arises from a mean-field instability whose existence depends on particle settling.

The imaginary part of each mode's growth rate is shown in figure 6 for $V = 10$. Fingering and γ-modes are direct (non-oscillatory) modes, contrary to the settling-driven large-scale modes. The oscillation frequency observed in the 'leaf' corresponding to the large-scale sedimentary instability increases rapidly with l and decreases with k. The frequencies associated with these oscillatory modes are discussed in detail in § 5.2.

The growth rate λ_{max} of the fastest-growing collective mode is computed from the flower plots by maximizing $\mathrm{Re}(\lambda)$ over all possible modes within the leaf and is presented in figure 7(*a*) as a function of V. We find that it grows with V and appears to go through a regime change at $V \approx 3$. This regime change is confirmed by looking at the wavenumbers of the most unstable mode (figure 7*b*), which also increase monotonically with V but whose dependence on V clearly changes at $V = 3$. Note that at $V = 5$, the wavenumbers of the fastest-growing mode are $(l_{max}, k_{max}) \approx (0.020, 0.033)$, such that the associated wavelengths remain much larger than individual fingers, and the mean-field theory assumptions are respected.

5.2. *Physical interpretation of the settling-driven collective instability*

Settling can play a dual role in the development of mean-field instabilities, as first noted by Reali *et al.* (2017). On the one-hand, it affects the development and nonlinear saturation of the basic instability, so that the properties of the small-scale turbulence vary with V. As a result, the mean-field parameters A_1, A_2 , Nu_0 and γ_0 all vary with V at otherwise fixed values of R_0, Pr and τ (see, e.g. table 1). On the other hand, settling also directly

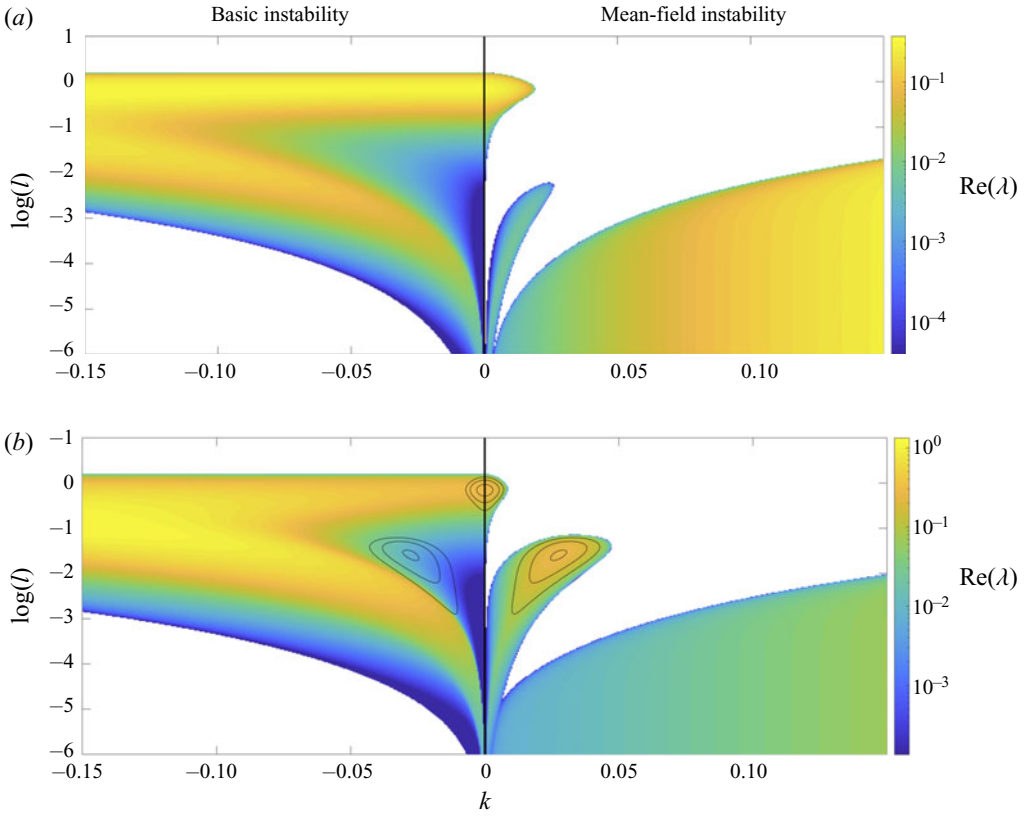

FIGURE 5. Real part of growth rates $\mathrm{Re}(\lambda)$ for the fastest-growing perturbations for Σ_{num} with $V = 2$ (*a*) and $V = 10$ (*b*). The left-hand side is calculated using the basic instability equation (3.2) while the right-hand side corresponds to the growth rates calculated using the generalized mean-field theory cubic, see (3.25). Here, we use the symmetry with respect to $k = 0$ to only represent half of the wavenumber space of each solution. The black lines represent the 0.1, 0.2 and 0.3 contours of the growth rate predicted by mean-field theory, superimposed on both sides of the plot.

affects the development of mean-field instabilities by causing a gradual phase shift of the large-scale particle and salinity fields with respect to one another, that is mathematically captured by the $-\mathrm{i}kV$ terms in (3.25). In order to isolate the contributions of each process to the development of mean-field modes in our system, we now consider four different cases where we compute the maximum positive real part of the solution to the cubic (3.25) with settling velocity $V = V_1$ but with mean-field parameters computed from a small-scale simulation at $V = V_2$, denoted $\mathrm{mfp}(V = V_2)$. We present in figure 8 the results for (*a*) $V_1 = 0$, $V_2 = 0$; (*b*) $V_1 = 2$, $V_2 = 0$; (*c*) $V_1 = 2$, $V_2 = 2$, and (*d*) $V_1 = 0$, $V_2 = 2$. The cases where $V_1 = V_2 = 0$ show the results of the mean-field theory in the absence of settling, while the case with $V_1 = V_2 = 2$ show those for $V = 2$. These reproduce the results shown in figure 6, for ease of comparison. The middle cases, with $V_1 \neq V_2$ are artificially investigated to isolate the effect of settling alone, and of the modified turbulence alone, on the stability of the sedimentary system.

First, no collective instability is observed when $V_1 = 0$ in the cubic equation with $\mathrm{mfp}(V_2 = 2)$, similarly to the case in which $V_1 = 0$ and $\mathrm{mfp}(V_2 = 0)$. This shows that

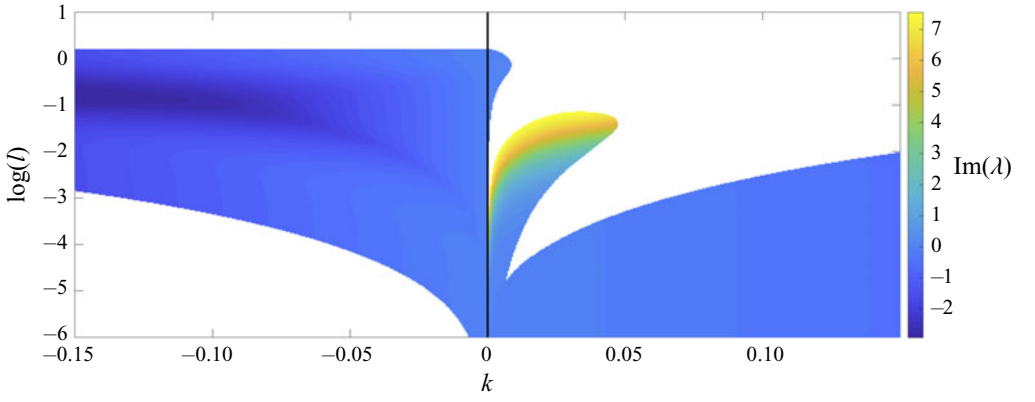

FIGURE 6. Imaginary part of growth rates $\mathrm{Im}(\lambda)$ for the fastest-growing perturbations for Σ_{num} with $V = 10$. The left-hand side is calculated using the basic instability cubic equation (3.2) while the right-hand side corresponds to the generalized mean-field theory (3.25). Here, we use the symmetry with respect to $k = 0$ to only represent half of the wavenumber space of each solution.

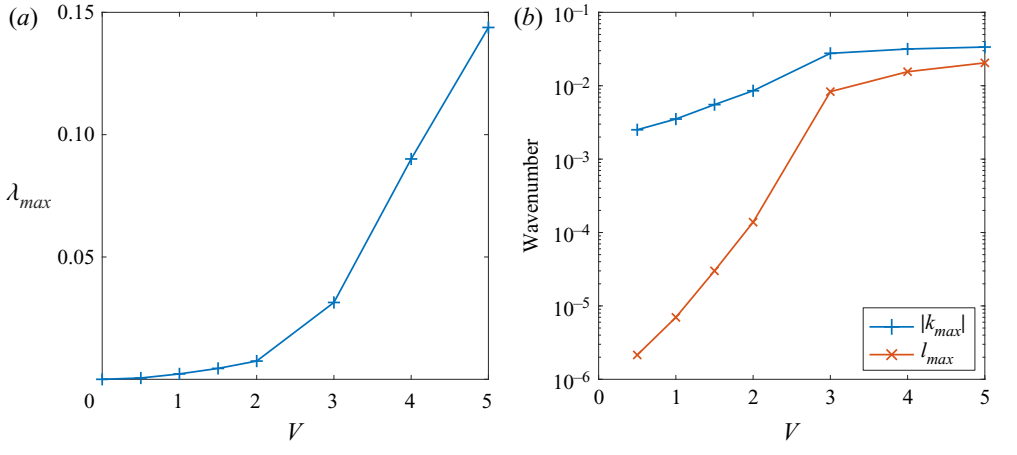

FIGURE 7. (*a*) Growth rate λ_{max} of the fastest-growing collective mode, i.e. the fastest growing mode of the large-scale settling driven collective instability, as a function of settling velocity V for the Σ_{num} parameters. (*b*) Horizontal wavenumber l_{max} and vertical wavenumber $|k_{max}|$ of the fastest-growing collective mode as a function of settling velocity V.

for such a settling speed, the change in turbulent properties induced by settling does not lead to the collective instability. More interestingly, setting $V_1 = 2$ with $\mathrm{mfp}(V_2 = 0)$ leads to the formation of a leaf of collectively unstable modes, despite the fact that we are using mean-field parameters calculated in the absence of settling. This suggests that the phase shift between the particle and salinity fields is the term responsible for destabilizing the system. Finally, by comparing the case with $V_1 = 2$, $\mathrm{mfp}(V_2 = 2)$ to the case with $V_1 = 2$, $\mathrm{mfp}(V_2 = 0)$ we see that that changes in the turbulence due to settling increase the range and growth rate of the new collective instability.

Particular attention must be paid to the sign of the imaginary part of the settling-driven collective mode. By contrast with the classic collective instability, which admits both

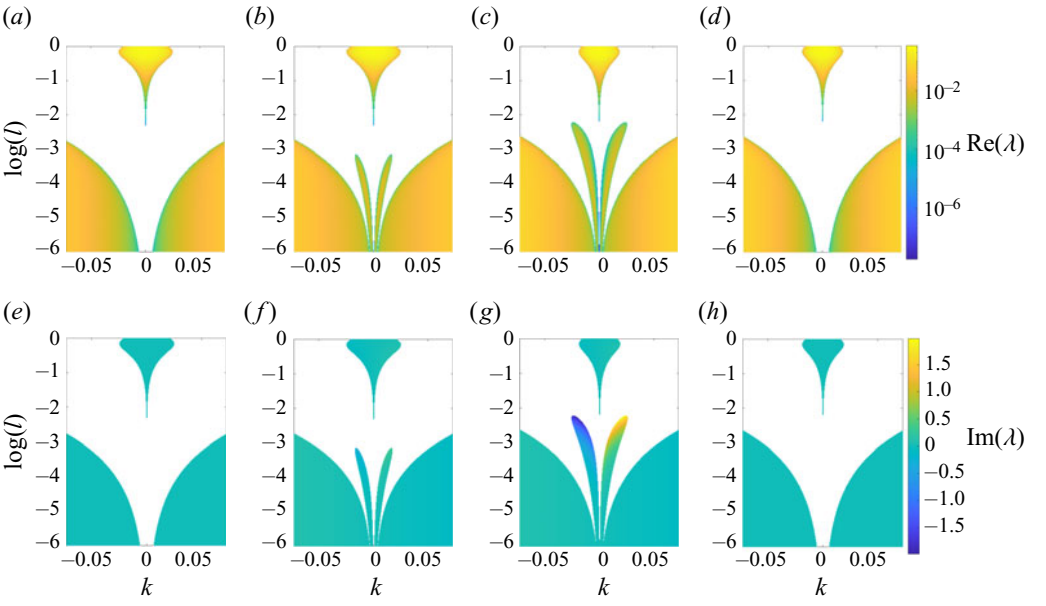

FIGURE 8. Real and imaginary parts of the fastest-growing solution to the generalized cubic equation (3.25) for the Σ_{num} parameters for various combinations of settling velocity V_1 and mean-field parameters mfp(V_2) computed from small-scale simulations that use a settling velocity V_2. (*a*,*e*) $V_1 = 0$, mfp($V_2 = 0$), (*b*,*f*) $V_1 = 2$, mfp($V_2 = 0$), (*c*,*g*) $V_1 = 2$, mfp($V_2 = 2$), (*d*,*h*) $V_1 = 0$, mfp($V_2 = 2$).

negative and positive solutions for the imaginary part of the fastest-growing mode, the sign of the frequency in the settling-driven mode depends on the sign of k (see figures 8*d* and 8*e–h*).

Figure 9 shows the same information as figure 8 but for a settling velocity of $V_1 = 10$ instead of $V_1 = 2$. This time, we see that a case with $V_1 = 0$, mfp($V_2 = 10$) does exhibit a collective instability when it did not for the $V_1 = 0$, mfp($V_2 = 2$) case, suggesting that for sufficiently high settling rates, the turbulence is substantially modified and becomes collectively unstable even when $V_1 = 0$. It is interesting to note that the collectively unstable modes induced solely by modified turbulence behave much like the classical collective instability, in that the sign of the imaginary part does not depend on k (see figures 9*c* and 9*e–h*).

This suggests that the regime change observed in figure 7 for the growth rate and most unstable wavenumbers of the collective mode reflects a change in the relative contribution of the two processes by which settling affects their development. At low settling speeds, the turbulence is generally unchanged from the non-sedimentary case, but the non-zero settling term in the cubic equation leads to a new mean-field instability. At high settling speeds, the changes in the turbulence properties induced by settling become substantial and drive the growth of collectively unstable modes in the classical sense, while the presence of settling in the cubic equation simply forces the sign of the imaginary part. The underlying mechanisms governing these two regimes are now described in more detail.

5.2.1. *Low settling velocity regime*

A simple interpretation for the emergence of the settling-driven collective mode at small settling velocities is found by investigating the stability of inclined gravity waves in the

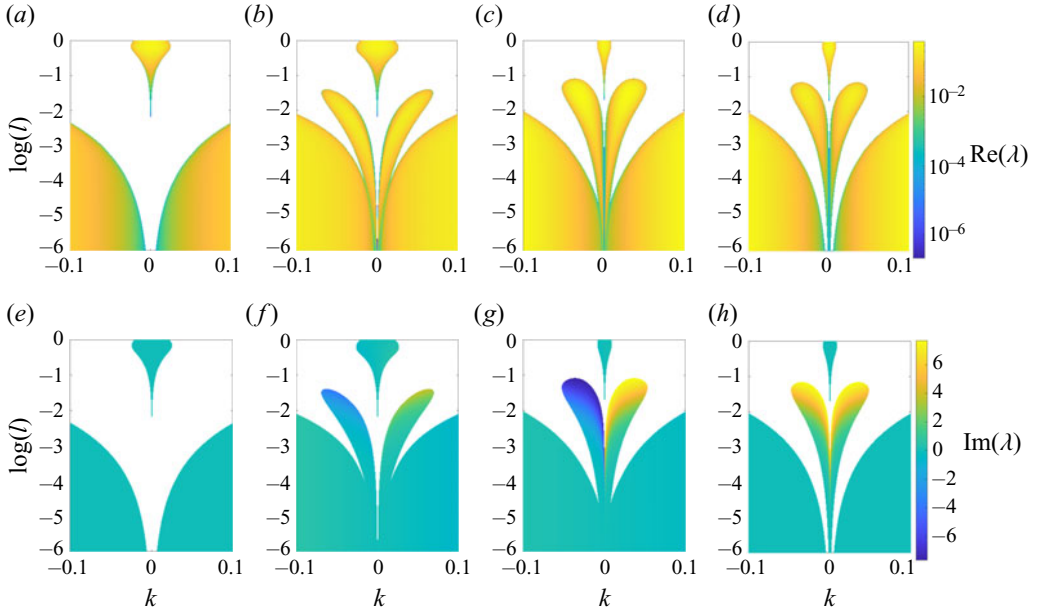

FIGURE 9. Real and imaginary parts of the fastest-growing solution to the generalized cubic equation (3.25) for the Σ_{num} parameters for various combinations of settling velocity V_1 and mean-field parameters mfp(V_2) computed from small-scale simulations that use a settling velocity V_2. (*a*,*e*) $V_1 = 0$, mfp($V_2 = 0$), (*b*, *f*) $V_1 = 10$, mfp($V_2 = 0$), (*c*,*g*) $V_1 = 10$, mfp($V_2 = 10$), (*d*,*h*) $V_1 = 0$, mfp($V_2 = 10$).

presence of two density-contributing fields where one settles under the effect of gravity while the other one does not. We further assume, as is the case here, that the non-settling field is stably stratified while the settling field is unstably stratified. As will be shown, diffusion is not necessary for this instability mechanism to operate, so it is entirely distinct from the double-diffusive instability discussed earlier in this work. On the other hand, it is essentially the same mechanism that destabilizes a doubly stratified particle-scalar system at density ratios $R_0 > 1/\tau$ (see Alsinan *et al.* 2017). The linearized equations governing this system are

$$\nabla \cdot \bar{\boldsymbol{u}} = 0, \tag{5.1}$$

$$\frac{1}{Pr}\frac{\partial \bar{\boldsymbol{u}}}{\partial t} = -\nabla \bar{p} + (\bar{\Theta} - \overline{C})\boldsymbol{e}_y, \tag{5.2}$$

$$\frac{\partial \overline{C}}{\partial t} + \frac{\bar{v}}{R_0} - V\frac{\partial \overline{C}}{\partial y} = 0, \tag{5.3}$$

$$\frac{\partial \bar{\Theta}}{\partial t} + \bar{v} = 0. \tag{5.4}$$

Using normal modes in the form $(\bar{u}, \bar{v}, \bar{p}, \bar{\Theta}, \overline{C}) \sim \mathrm{Re}((\hat{u}, \hat{v}, \hat{p}, \hat{\Theta}, \hat{C})\exp(\lambda t + \mathrm{i}lx + \mathrm{i}ky))$, we find the growth rate cubic equation

$$\lambda^3 + \lambda^2(-\mathrm{i}kV) + \lambda Pr\frac{l^2}{|\boldsymbol{k}|^2}\left(1 - \frac{1}{R_0}\right) - Pr\frac{l^2}{|\boldsymbol{k}|^2}\mathrm{i}kV = 0. \tag{5.5}$$

Solutions of this cubic equation with positive real part exist for a range of k and l, demonstrating that this simple system is indeed unstable. The growth rate (*a–d*) and corresponding imaginary part (*e–h*) are plotted as functions of k and l in figure 10 for $R_0 = 1.5$, $Pr = 200$ and various values of V. We see that unstable inclined gravity waves are excited as soon as $V \neq 0$. This instability mechanism is easily understood physically (see sketch in figure 11): the inclined waves transport denser fluid upward, and lighter fluid downward. As the particle field settles, it contributes to increasing the density of the upward moving fluid relative to the downward moving lighter fluid. Once the direction of the inclined wave reverses, the dense fluid thus overshoots its former point of neutral buoyancy, and the instability is amplified. A similar argument can be applied for the lighter fluid regions. An intuitive condition for this amplification to occur is that the frequency associated with the settling of the particle field should be of the same order as the oscillation frequency of the gravity wave ω_w, i.e.

$$\omega_w = \sqrt{Pr\,(1 - 1/R_0)}\,\frac{l}{|\boldsymbol{k}|} \sim 2\pi k V. \tag{5.6}$$

If we restrict our analysis to modes for which $l \ll k$ such that $|\boldsymbol{k}|^2 \approx k^2$, the amplification condition becomes

$$l \sim 2\pi \frac{k^2 V}{\sqrt{Pr\,(1 - 1/R_0)}}. \tag{5.7}$$

This relationship is shown as the red line in figure 10. We observe that the amplification condition agrees very well with the maximum value of l (for a given k) below which the modes grow. We therefore postulate that a simple approximate condition for the growth of the new settling-driven instability in the low settling velocity regime can be derived from (5.7).

In order to test this hypothesis, we first compare the fastest-growing mode growth rate and wavenumbers obtained from the solution of the general mean-field cubic equation (3.25) using $V_1 = V_2 = V$, to that obtained using $V_1 = V$ but $V_2 = 0$ (see § 5.2 for definitions of V_1 and V_2). We see in figure 12 that the two are very close for low V, confirming that the dynamics of the settling-driven collective instability is controlled by the settling-induced phase shift between the particle and salinity fields. More importantly, we also see that the solutions obtained by setting $V_2 = 0$ scale as an exact power law of V, with $\lambda(V) = \hat{\lambda} V^2$, $k(V) = \hat{k} V$ and $l(V) = \hat{l} V^3$.

As we now demonstrate, these scalings are a direct consequence of the amplification condition (5.7). Indeed, let us assume that λ, k and l scale as

$$\lambda = \hat{\lambda} V^{\mu}, \quad k = \hat{k} V^{\chi}, \quad l = \hat{k}^2 V^{2\chi+1}, \tag{5.8a–c}$$

where we have used the scalings suggested by (5.7) to relate the ansatz for k to the one for l. The exponents χ and μ are uniquely determined by requiring that λ be a solution of (3.25). Indeed, for the scaled growth rate $\hat{\lambda}$ to be independent of V, the scaling

$$V^{3\mu} \sim a_2(V) V^{2\mu} \sim a_1(V) V^{\mu} \sim a_0, \tag{5.9}$$

must hold true. Here, a_2, a_1, a_0 are the coefficients given in (3.26)–(3.28), which are functions of V via k and l. For small wavenumber k, under the amplification condition (5.7), we have $l \ll k$ so that $|\boldsymbol{k}|^2 \approx k^2$. From a scaling perspective,

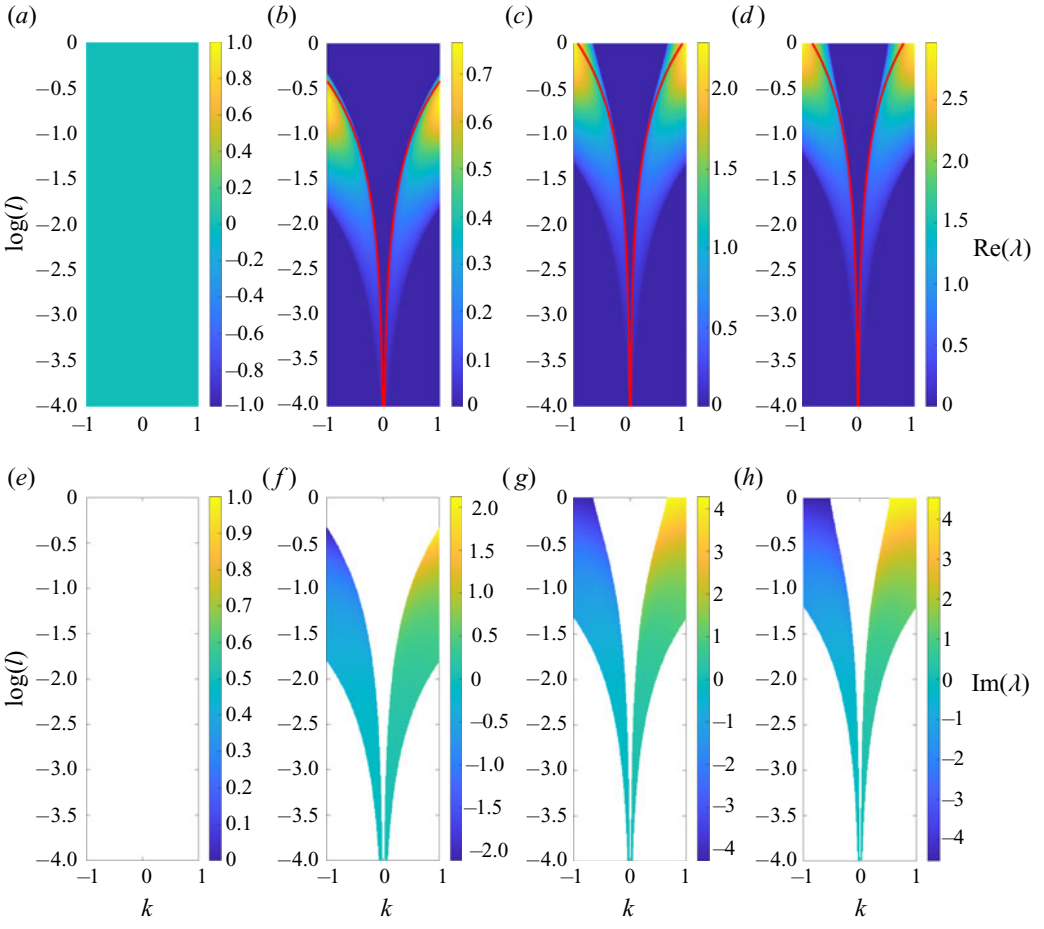

FIGURE 10. (*a–b*) Growth rate of instability in a linearly stratified fluid in the presence of a settling destabilizing field and a non-settling stabilizing field, see § 5.2.1. (*e–f*) Corresponding imaginary part to the fastest-growing mode under the condition $\mathrm{Re}(\lambda > 10^{-12})$. Here, $R_0 = 1.5$, $Pr = 200$. (*a*,*e*) $V = 0$, (*b*, *f*) $V = 0.5$, (*c*,*g*) $V = 1.5$, (*d*,*h*) $V = 2$.

this implies that

$$a_2 \sim \hat{k}^2 V^{2\chi} - \mathrm{i}\hat{k} V^{\chi+1}, \tag{5.10}$$

$$a_1 \sim \hat{k}^4 V^{4\chi} - \mathrm{i}\hat{k}^3 V^{3\chi+1} + \hat{k}^2 V^{2\chi+2}, \tag{5.11}$$

$$a_0 \sim \hat{k}^6 V^{6\chi} + \hat{k}^4 V^{4\chi+2} - \mathrm{i}\hat{k}^3 \left(V^{5\chi+1} + V^{3\chi+3}\right). \tag{5.12}$$

The constraint of (5.9) is easily verified to hold when $\mu = 2$ and $\chi = 1$, which are the numerically computed scalings observed in figure 12. This shows that the amplification condition (5.7) does indeed capture the mechanism that leads to the destabilization of inclined gravity waves.

5.2.2. *High settling velocity regime*

The growth rate of the collective modes in the high-V limit (for instance, at $V = 10$) is almost identical when computed using the true mean-field parameters (mfp($V_2 = 10$))

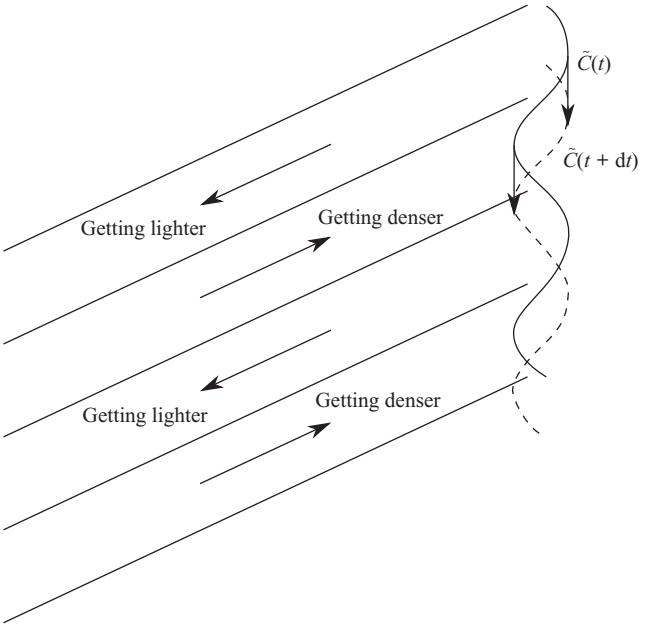

FIGURE 11. Sketch of the gravity wave amplification mechanism in the presence of a settling destabilizing field and a non-settling stabilizing field (see main text for detail).

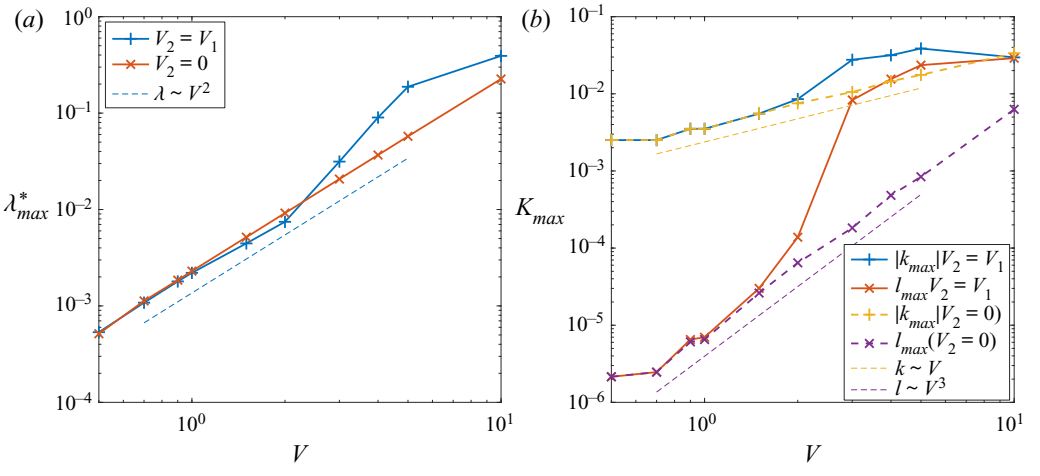

FIGURE 12. (*a*) Growth rate λ_{max} of the fastest-growing collective mode as a function of settling velocity V, using $V_1 = V$ with either $V_2 = V$ or $V_2 = 0$. (*b*) Horizontal wavenumber l_{max} and vertical wavenumber $|k_{max}|$ of the fastest-growing collective mode as a function of settling velocity V, using $V_1 = V$ with either $V_2 = V$ or $V_2 = 0$. In both panels, $R_0 = 1.5$, $Pr = 200$ and $\tau = 0.1$.

regardless of whether V_1 is set to 0 or 10 in the cubic equation (3.25) (see figure 9*c*,*d*). In the high-V regime, we therefore conclude that the settling-induced changes to the small-scale turbulence are the primary cause of the emergent mean-field mode, and that this mode is unstable to the collective instability in the classic sense of Stern *et al.* (2001) and Traxler *et al.* (2011). A physical interpretation for the collective instability was

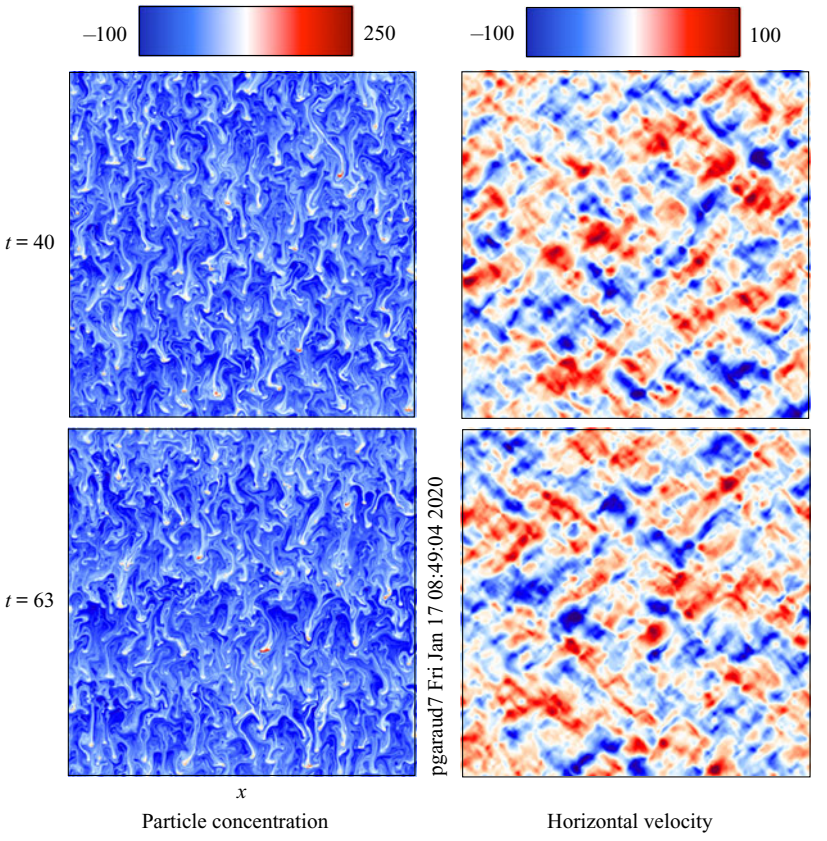

FIGURE 13. Snapshot of particle concentration $\tilde{C}$ and horizontal velocity u at $t = 40$ and $t = 63$ for a large-scale simulation of the Σ_{num} system at $V = 5$.

proposed by Stern *et al.* (2001), who identified the variations in salt-finger buoyancy flux induced by the wave to feed the instability. The only effect of settling on the development of that instability seems to be to damp the mode that opposes the direction of settling, and to reinforce the mode that acts in the direction of settling. Thus, settling simply restricts the sign of the imaginary part of λ. This is observed directly in figure 9(*e–h*). The imaginary part of the growth rate in the case where the cubic equation is solved with $V_1 = 0$ and mfp($V_2 = 10$) can either be negative or positive, and does not depend on the sign of k. This contrasts with the solution at $V_1 = 10$ and mfp($V_2 = 10$), where the imaginary part only admits one solution for the fastest growing mode, that depends on the sign of k.

5.3. *DNS of the collective instability in sedimentary fingering convection*

The new settling-driven collective instability, predicted to exist at low settling velocity, only grows for very small wavenumbers, and has a very small growth rate. With present computational power, it is not possible to resolve domains large enough over adequately large simulation times to capture this new instability. We can, however, show the ability of settling to excite the classical collective instability in the high settling velocity regime. To do so, we conduct large-domain DNS of the sedimentary system Σ_{num} at $V = 5$ and $V = 10$ in order to verify whether the gravity waves predicted by mean-field theory indeed grow. At $V = 5$ and $V = 10$, the predicted growth rates of the fastest-growing

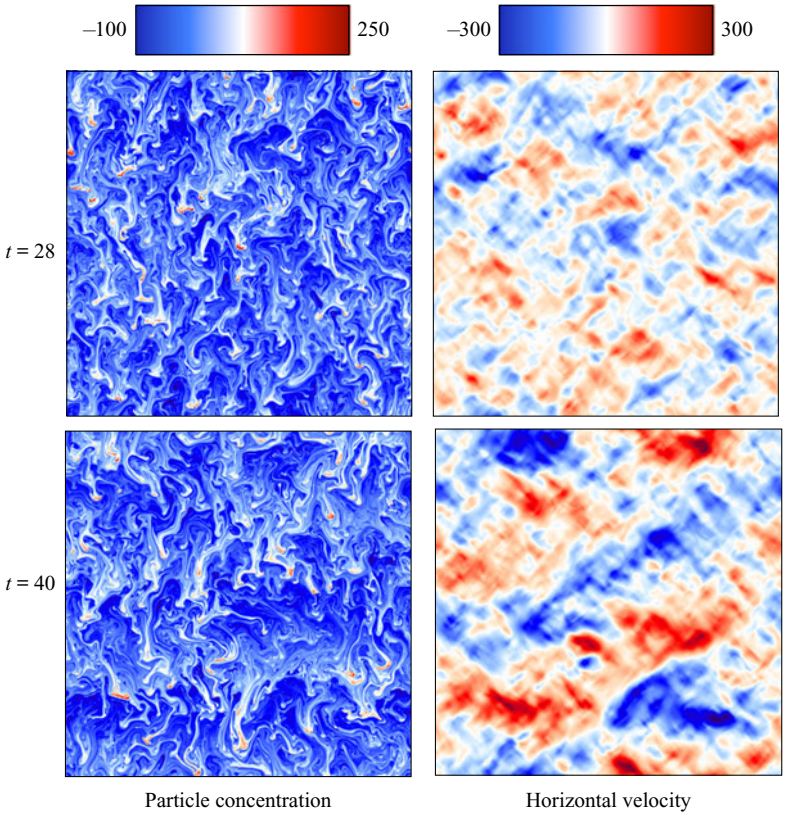

FIGURE 14. Snapshots of the particle concentration $\tilde{C}$ and horizontal velocity u at $t = 28$ and $t = 40$ for a large-scale simulation of the Σ_{num} system at $V = 10$.

modes of the collective instability are 0.1875 and 0.3920, respectively. The corresponding wavenumbers are $(l_{max}, k_{max}) = (0.0235, 0.0387)$ and $(l_{max}, k_{max}) = (0.0290, 0.0296)$, respectively, corresponding to wavelengths of $(2\pi/k_{max}, 2\pi/l_{max}) = (267.36, 162.36)$ and $(2\pi/k_{max}, 2\pi/l_{max}) = (216.66, 212.27)$, respectively. The domain size is therefore set to 400×400 such that at least one wavelength of the instability should be able to grow. The simulations are run using the PADDI code (Stellmach *et al.* 2011; Traxler *et al.* 2011; Reali *et al.* 2017) on 4608×4608 equivalent grid points. Figures 13 and 14 show snapshots of the particle concentration and horizontal velocity at two different times for $V = 5$ and $V = 10$, respectively. At $V = 5$, the system appears to transition from a state of saturated fingering directly to a layered state, with layers visible at $t = 63$ in the particle concentration field. Note that layering in the presence of settling occurs much earlier than in the absence of settling (see figure 3). The absence of collective modes in this case is likely due to their small growth rates, as they do not have time to grow before the layering instability takes over. At $V = 10$, however, large inclined structures are temporarily seen to appear in the state of saturated fingering around $t = 40$. While diagonal lines of fingers can be perceived in the particle concentration snapshot, this is most clearly observed in the horizontal velocity snapshot, with clear alternating layers of left- and right-propagating fluid. It can be inferred that the angle of the inclined wave with the horizontal is slightly less than 45°, which compares qualitatively well with the predicted angle $\arctan(l_{max}/k_{max}) \approx 44.4°$ at $V = 10$.

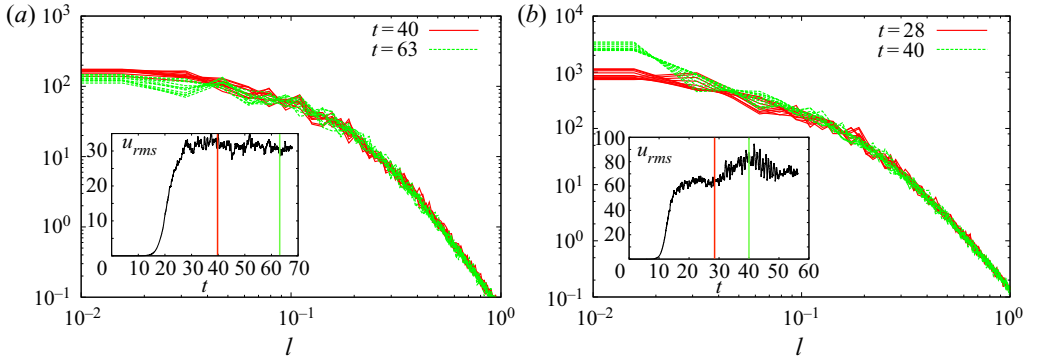

FIGURE 15. Horizontal spectra of horizontal velocity in large-scale simulations of Σ_{num} for $V = 5$ (a) and $V = 10$ (b). The inset shows the r.m.s. horizontal velocity as a function of time, with vertical lines marking the times around which the spectra are taken. The various lines in the spectra correspond to different time steps around the times indicated in the legend.

Additional evidence for the growth of inclined waves can be found in the horizontal spectra of horizontal velocity, defined as $Q(l) = \sum_k \hat{U}(l,k)\hat{U}^*(l,k)$, where $\hat{U}$ is the Fourier transform of the horizontal velocity u. It is plotted as a function of the horizontal wavenumber in figure 15 for $V = 5$ and $V = 10$. In both cases, the spectra are taken around the same times as the snapshots shown in figures 13 and 14, with different lines corresponding to nearby time-steps as an indicator of their intrinsic temporal variability. At $V = 5$, there is no discernible change in the spectra between $t = 40$ and $t = 63$ at the lowest wavelengths, which correspond to the fastest-growing gravity wave mode predicted by mean-field theory. At $V = 10$, however, a noticeable increase in energy in the low wavenumber modes is observed at $t = 40$, corresponding to the time at which coherent inclined structures can be observed in the snapshots (see figure 14). This suggests that the collective instability predicted by the mean-field theory indeed is excited, but only for sufficiently large settling velocities, so that the gravity waves grow faster than the layers. The layers eventually grow as well, however, and suppress the waves when they do (e.g. around $t = 50$ in the $V = 10$ simulation).

6. Conclusion

The mean-field theory approach has been successfully employed to describe layering in non-sedimentary (Radko 2003) and sedimentary fingering convection (Reali *et al.* 2017), as well as to recover the collective instability of Stern *et al.* (2001) and intrusive mode or intrusions of Walsh & Ruddick (1995) (see also Traxler *et al.* 2011). However, none of these studies considered high-Prandtl-number sedimentary systems, which are commonly associated with a particle-laden salt-stratified water column. In this work, we extended the mean-field theory of Traxler *et al.* (2011) to include sedimentation, in which the unstably stratified diffusing scalar settles at a constant non-dimensional velocity $V = V_{st}d/\kappa_s$ (see § 2.2). We analysed the mean-field stability of fingering convection at high Prandtl number, both in the presence and absence of settling. We found that non-sedimentary systems can be collectively stable, yet unstable to layering, and confirmed our theory with DNS. We additionally found that high wavenumber layering modes (which would result in closely spaced layers) do not grow at all in the DNS, while the more widely spaced layers that are observed to form do not grow at the rate predicted by the mean-field theory.

This discrepancy was already noted by Reali *et al.* (2017), who suggested that larger wavenumber modes may be filtered by the presence of vertically elongated fingers. This hypothesis could in the future be tested by running simulations in much larger domains.

In the presence of settling, this picture changes markedly. Just as Reali *et al.* (2017) found for the layering instability, we have identified two pathways to the collective instability in the presence of settling. At low settling velocities, the turbulence is relatively unaffected by settling, and the system remains collectively stable in the classical sense of Stern *et al.* (2001). However, settling induces a new type of instability by amplifying inclined gravity waves. The amplification occurs when the wave oscillation period is of the same order as the particle settling time scale through the wave. In this case, we have found that the growth rate, horizontal wavenumber and vertical wavenumber of the wave scale as V^2, V^3 and V, respectively. At higher settling velocities, on the other hand, the sedimentary dynamics changes the turbulent properties of the flow such that it becomes collectively unstable in the classical sense.

Our model makes interesting predictions for possible future experiments on sedimentary double-diffusive convection. Indeed, considering a fiducial stratification of $N \sim 10^{-2}\ \mathrm{s}^{-1}$, the dimensional diffusive time scale $T = d^2/\kappa$ (see § 2.2) is respectively about 6 minutes for the heat-particle system and 1 h for the salt–particle system. An interesting side effect of such a slow diffusive time scales in the salt–particle system is that the diffusive velocity scale ($U = \kappa_s/d \sim 5.6 \times 10^{-7}\ \mathrm{m\,s}^{-1}$) is very small and thus even small particles have large non-dimensional settling velocities. We take the example of particles of size $d_p \sim 2.6\ \mu\mathrm{m}$ settling at $V_{st} \sim 5.6 \times 10^{-6}\ \mathrm{m\,s}^{-1}$ (i.e. at a non-dimensional velocity $V = V_{st}/U \sim 10$). In a 2 m water column, these particles would require close to 100 h to settle entirely. Even though they were run at slightly smaller Prandtl number ($Pr = 200$) than for a real salt–particle system (which would be closer to $Pr = 1000$), our DNS results (figure 14) suggest that at such settling speeds, layering could be expected to occur after only 45 h (non-dimensional time $t = t^*/T \sim 50$). This suggests that settling processes play a much more prevalent role in salt-stratified double-diffusive convection than in heat-stratified systems. Note that taking d as the eddy size and considering an eddy velocity of $300\kappa_s/d$ (see figure 14), we find that $St \approx 3 \times 10^{-8} \ll 1$. For the parameters considered, the Stokes number (see § 2) is thus very small and the equilibrium Eulerian assumption holds.

It is thus very likely that observations of settling-driven layering could be made in salt-stratified environments in which particle-laden fluid is released, which is particularly pertinent to the experiments of Carazzo & Jellinek (2013). Indeed, the authors used particles of mean diameter 300 μm, thus having a Stokes settling speed of order $V_{st} \sim 0.075\ \mathrm{m\,s}^{-1}$ (or $V = V_{st}/U \sim 10^5$). While such a regime is computationally inaccessible to current technology, the present study suggests that settling would markedly impact the turbulence properties and significantly increase the growth rate of both gravity waves and layers. We thus argue that while classic double-diffusive convection theory does not explain layering at the density ratios considered in the Carazzo and Jellinek experiments, the present theory does. A follow-up study to these experiments with much smaller particles would allow direct testing of the theory presented above, and offer the possibility of a direct comparison with numerical simulations.

The new settling-driven collective instability, that only exists for small values of V, might prove far more challenging to observe experimentally. At the Σ_{num} parameters with $V = 1$, the non-dimensional growth rate of the new instability is estimated to be $\lambda = 0.0022$. With the same fiducial values as before, i.e. $T \approx 1$ h, the characteristic growth time is $T/\lambda \sim 450$ h. With a fiducial $U = \kappa_s/d \sim 5.6 \times 10^{-7}\ \mathrm{m\,s}^{-1}$, the vertical

displacement of the particles is less than 1 m over that time. The time particles take to settle over vertical distances typical of oceanic environments is thus unlikely to be a limiting factor in the growth of this novel instability. The horizontal wavelength of the fastest-growing mode, on the other hand, is estimated to be of order $l_{max}/d \sim 200$ m. The existence of a system sufficiently large and that remains otherwise quiescent over sufficiently long times for this instability to grow seems extremely unlikely, at least on Earth. In addition, for the Σ_{num} parameters, the γ-instability always grows faster than the new collective instability, which precludes us from observing it. However, the growth rate of the γ-instability depends strongly on the rate of decrease of γ with respect to R_0, which decreases as R_0 increases (Traxler *et al.* 2011). As such, more stably stratified systems might be better suited to observe the novel collective instability by delaying or suppressing layering.

Acknowledgements

This research has been supported by NSF grant CBET-1438052 to E.M., and by grant NSF CBET-1437275 to P.G., as well as through Army Research Office Grant No. W911NF-18-1-0379 to E.M. This work used the Extreme Science and Engineering Discovery Environment (XSEDE), which is supported by National Science Foundation grant number ACI-1053575.

Declaration of interests

The authors report no conflict of interest.

Appendix A. Protocol for computing mean-field parameters

Following the method of Traxler *et al.* (2011), we determine the Nusselt number and flux ratio for selected values of Pr, τ, R_0 and V by running small-scale two-dimensional simulations. The size of the domain was selected as follows: it has to be large enough to fit a few fingers so as to provide good statistical estimates of the fluxes but at the same time should not be too large lest secondary instabilities appear. In the absence of settling, we ran our small-scale simulations in a domain of 5×10 fgw, or equivalently 37×74 units. In the presence of settling, we ran the small-scale simulations in 100×100 boxes. These choices, following Radko (2003) and Reali *et al.* (2017), are purely empirical but seem to be a good compromise.

In order to perturb the system from the linearly stratified base state, we initiate all fields with low-amplitude white noise. The system is evolved until a statistically stationary state is reached. We then perform a time average of the turbulent fluxes in that state, and measure their r.m.s. fluctuations to estimate their natural variability.

For each set of parameters, additional simulations are run with a slightly greater density ratio $R_0 + \mathrm{d}R$ and a slightly lower density ratio $R_0 - \mathrm{d}R$ such that an estimate for the first derivative of the Nusselt number and of the inverse flux ratio can be derived as

$$\frac{\mathrm{d}Nu}{\mathrm{d}R_\rho}(R_0) = \frac{Nu(R_0 + \mathrm{d}R) - Nu(R_0 - \mathrm{d}R)}{2\mathrm{d}R} + O(dR^2), \tag{A 1}$$

$$\frac{\mathrm{d}(1/\gamma)}{\mathrm{d}R_\rho} = \frac{\dfrac{1}{\gamma(R_0 + \mathrm{d}R)} - \dfrac{1}{\gamma(R_0 - \mathrm{d}R)}}{2\mathrm{d}R} + O(\mathrm{d}R^2). \tag{A 2}$$

With this methodology, mean-field parameters of any system with given Pr, τ, R_0 and V can be computed by running three small-scale simulations. dR is set to 0.1 for the results presented in table 1. The quantity A_1^{tot}, defined as

$$A_1^{tot} = R_0 \frac{\mathrm{d}(1/\gamma^{tot})}{\mathrm{d}R_\rho}\bigg|_{R_0} \tag{A 3}$$

is a diagnostic for the γ-instability, with A_1^{tot} being positive signifying that the system is unstable to layering.

REFERENCES

ALSINAN, A., MEIBURG, E. & GARAUD, P. 2017 A settling-driven instability in two-component, stably stratified fluids. *J. Fluid Mech.* **816**, 243–267.

BAINES, P. G. & GILL, A. E. 1969 On thermohaline convection with linear gradients. *J. Fluid Mech.* **37** (2), 289–306.

BURNS, P. & MEIBURG, E. 2012 Sediment-laden fresh water above salt water: linear stability analysis. *J. Fluid Mech.* **691**, 279–314.

BURNS, P. & MEIBURG, E. 2015 Sediment-laden fresh water above salt water: nonlinear simulations. *J. Fluid Mech.* **762**, 156–195.

CANUTO, C., HUSSAINI, M. Y., QUARTERONI, A. & ZANG, T. A. 2007 *Spectral Methods in Fluid Dynamics*. Springer.

CARAZZO, G. & JELLINEK, M. A. 2013 Particle sedimentation and diffusive convection in volcanic ash-clouds. *J. Geophys. Res.* **118** (4), 1420–1437.

DAVARPANAH JAZI, S. & WELLS, M. G. 2016 Enhanced sedimentation beneath particle-laden flows in lakes and the ocean due to double-diffusive convection. *Geophys. Res. Lett.* **43** (20), 10883–10890.

DAVIS, R. H. 1996 Hydrodynamic diffusion of suspended particles: a symposium. *J. Fluid Mech.* **310**, 325–335.

FERRY, J. & BALACHANDAR, S. 2001 A fast Eulerian method for disperse two-phase flow. *Intl J. Multiphase Flow* **27** (7), 1199–1226.

GARAUD, P. 2018 Double-diffusive convection at low Prandtl Number. *Annu. Rev. Fluid Mech.* **50** (1), 275–298.

GARAUD, P., MEDRANO, M., BROWN, J. M., MANKOVICH, C. & MOORE, K. 2015 Excitation of gravity waves by fingering convection, and the formation of compositional staircases in stellar interiors. *Astrophys. J.* **808** (1), 1–14.

GREEN, T. 1987 The importance of double diffusion to the settling of suspended material. *Sedimentology* **34** (2), 319–331.

HOLYER, J. Y. 1981 On the collective instability of salt fingers. *J. Fluid Mech.* **110**, 195–207.

HOUK, D. & GREEN, T. 1973 Descent rates of suspension fingers. *Deep-Sea Res. Oceanogr. Abstr.* **20** (8), 757–761.

KRISHNAMURTI, R. 2003 Double-diffusive transport in laboratory thermohaline staircases. *J. Fluid Mech.* **483**, 287–314.

KUNZE, E. 2003 A review of oceanic salt-fingering theory. *Prog. Oceanogr.* **56** (3–4), 399–417.

LINDEN, P. 1973 On the structure of salt fingers. *Deep-Sea Res. Oceanogr. Abstr.* **20** (4), 325–340.

MERRYFIELD, W. J. 2000 Origin of thermohaline staircases. *J. Phys. Oceanogr.* **30** (5), 1046–1068.

PEYRET, R. 2002 *Spectral methods for incompressible viscous flow*. Applied Mathematical Sciences, vol. 148. Springer.

POISSON, A. & PAPAUD, A. 1983 Diffusion coefficients of major ions in seawater. *Mar. Chem.* **13** (4), 265–280.

RADKO, T. 2003 A mechanism for layer formation in a double-diffusive fluid. *J. Fluid Mech.* **497**, 365–380.

RADKO, T. 2013 *Double-Diffusive Convection*. Cambridge University Press.

RADKO, T. & SMITH, D. P. 2012 Equilibrium transport in double-diffusive convection. *J. Fluid Mech.* **692**, 5–27.

RANI, S. L. & BALACHANDAR, S. 2003 Evaluation of the equilibrium Eulerian approach for the evolution of particle concentration in isotropic turbulence. *Intl J. Multiphase Flow* **29** (12), 1793–1816.

REALI, J. F., GARAUD, P., ALSINAN, A. & MEIBURG, E. 2017 Layer formation in sedimentary fingering convection. *J. Fluid Mech.* **816**, 268–305.

RUDNICK, D. L. 1999 Compensation of horizontal temperature and salinity gradients in the ocean mixed layer. *Science* **283** (5401), 526–529.

SCHMITT, R. W. 1979 The growth rate of super-critical salt fingers. *Deep-Sea Res.* I **26** (1), 23–40.

SCHMITT, R. W. 1994 Double diffusion in oceanography. *Annu. Rev. Fluid Mech.* **26** (1), 255–285.

SCHMITT, R. W., PERKINS, H., BOYD, J. D. & STALCUP, M. C. 1987 C-SALT: an investigation of the thermohaline staircase in the western tropical North Atlantic. *Deep-Sea Res.* I **34** (10), 1655–1665.

SHEN, C. Y. & SCHMITT, R. W. 2013 The salt finger wavenumber spectrum. In *Double-Diffusive Convection* (eds A. Brandt & H. Fernando). doi:10.1029/GM094p0305.

STELLMACH, S. & HANSEN, U. 2008 An efficient spectral method for the simulation of dynamos in Cartesian geometry and its implementation on massively parallel computers. *Geochem. Geophys. Geosyst.* **9** (5), 1–11.

STELLMACH, S., TRAXLER, A., GARAUD, P., BRUMMELL, N. & RADKO, T. 2011 Dynamics of fingering convection. Part 2. The formation of thermohaline staircases. *J. Fluid Mech.* **677**, 554–571.

STERN, M. E. 1960 The "salt-fountain" and thermohaline convection. *Tellus* **12** (2), 172–175.

STERN, M. E. 1969 Collective instability of salt fingers. *J. Fluid Mech.* **35** (02), 209–218.

STERN, M. E., RADKO, T. & SIMEONOV, J. 2001 Salt fingers in an unbounded thermocline. *J. Mar. Res.* **59** (3), 355–390.

SÁNCHEZ, X. & ROGET, E. 2007 Microstructure measurements and heat flux calculations of a triple-diffusive process in a lake within the diffusive layer convection regime. *J. Geophys. Res.* **112** (C2), C02012.

TAIT, R. I. & HOWE, M. R. 1968 Some observations of thermo-haline stratification in the deep ocean. *Deep-Sea Res. Oceanogr. Abstr.* **15** (3), 275–280.

TRAXLER, A., STELLMACH, S., GARAUD, P., RADKO, T. & BRUMMELL, N. 2011 Dynamics of fingering convection. Part 1. Small-scale fluxes and large-scale instabilities. *J. Fluid Mech.* **677**, 530–553.

TURNER, J. S. 1967 Salt fingers across a density interface. *Deep-Sea Res. Oceanogr. Abstr.* **14** (5), 599–611.

TURNER, J. S. 1974 Double-diffusive phenomena. *Annu. Rev. Fluid Mech.* **6** (1), 37–54.

WALSH, D. & RUDDICK, B. 1995 Double-diffusive interleaving: the influence of nonconstant diffusivities. *J. Phys. Oceanogr.* **25** (3), 348–358.

WHITFIELD, D. W. A., HOLLOWAY, G. & HOLYER, J. Y. 1989 Spectral transform simulations of finite amplitude double-diffusive instabilities in two dimensions. *J. Mar. Res.* **47** (2), 241–265.

YOU, Y. 2002 A global ocean climatological atlas of the Turner angle: implications for double-diffusion and water-mass structure. *Deep-Sea Res.* I **49** (11), 2075–2093.

YU, X., HSU, T. & BALACHANDAR, S. 2013 Convective instability in sedimentation: linear stability analysis. *J. Geophys. Res.* **118** (1), 256–272.

YU, X., HSU, T. & BALACHANDAR, S. 2014 Convective instability in sedimentation: 3-D numerical study. *J. Geophys. Res.* **119** (11), 8141–8161.